

Multireflection boundary conditions for lattice Boltzmann modelsIrina Ginzburg^{1,*} and Dominique d'Humières^{2,†}¹*Fraunhofer Institut für Techno und Wirtschaftsmathematik, Gottlieb-Daimler-Strasse 49, Kaiserslautern D-67663, Germany*²*Laboratoire de Physique Statistique de l'École Normale Supérieure, 24 Rue Lhomond, 75321 Paris Cedex 05, France*

(Received 15 October 2002; revised manuscript received 7 August 2003; published 31 December 2003)

We present a general framework for several previously introduced boundary conditions for lattice Boltzmann models, such as the bounce-back rule and the linear and quadratic interpolations. The objectives are twofold: first to give theoretical tools to study the existing link-type boundary conditions and their corresponding accuracy; second to design boundary conditions for general flows which are third-order kinetic accurate. Using these new boundary conditions, Couette and Poiseuille flows are exact solutions of the lattice Boltzmann models for a Reynolds number $Re=0$ (Stokes limit) for arbitrary inclination with the lattice directions. Numerical comparisons are given for Stokes flows in periodic arrays of spheres and cylinders, linear periodic array of cylinders between moving plates, and for Navier-Stokes flows in periodic arrays of cylinders for $Re < 200$. These results show a significant improvement of the overall accuracy when using the linear interpolations instead of the bounce-back reflection (up to an order of magnitude on the hydrodynamics fields). Further improvement is achieved with the new multireflection boundary conditions, reaching a level of accuracy close to the quasianalytical reference solutions, even for rather modest grid resolutions and few points in the narrowest channels. More important, the pressure and velocity fields in the vicinity of the obstacles are much smoother with multireflection than with the other boundary conditions. Finally the good stability of these schemes is highlighted by some simulations of moving obstacles: a cylinder between flat walls and a sphere in a cylinder.

DOI: 10.1103/PhysRevE.68.066614

PACS number(s): 47.11.+j, 47.45.-n, 05.20.Dd

I. INTRODUCTION

Boundary conditions in kinetic (or particle) methods, the lattice Boltzmann (LB) model being one such example, are fundamentally different from their equivalent for more traditional computational fluid dynamics (CFD) methods, such as finite-difference or finite-element ones. In many traditional CFD methods the boundary conditions (for instance fluid velocity, pressure, or some of their derivatives) are explicitly set on the nodes defining the mesh boundary. In kinetic methods, the particles (populations) leaving the computational domain have to be replaced by particles (populations) entering it. The properties of these entering particles define the boundary conditions and can be either given *a priori* or computed from those of the leaving particles. Such boundary conditions can only be set exactly from a perfect knowledge of the kinetic properties of the studied flow. In general this perfect knowledge is not available and some approximations have to be used, leading to some discrepancies between the particle distributions prescribed by the fluid dynamics and the boundary conditions. The resulting mismatch obviously limits the accuracy of modeling usual macroscopic boundary conditions by kinetic methods. It is well known in the context of rarefied gas dynamics that the physical effect of such mismatch creates a region, located near the boundary, where the discrepancy between the local distributions and the fluid ones is exponentially damped away from it (see, for instance,

Ref. [1]). This layer near the boundaries is known as the Knudsen or accommodation layer and leads at the macroscopic level to an apparent nonzero velocity at the boundary (slip velocity). Moreover, in numerical methods using an underlying grid, the actual boundaries are not located on the grid points but at positions depending upon the details of the boundary conditions.

It has been recognized quite early that such effects indeed exist in lattice gases and lattice Boltzmann equation. In Ref. [2] Knudsen layers have been studied for two simple orientations of the boundary on a triangular lattice and it has been shown for Couette flows that the bounce-back condition locates the no-slip walls midway through the last fluid node and the first outside one. This result has been extended in Refs. [3,4] to Poiseuille-Hagen flows for which it has been shown that exact parabolic profiles, for the same no-slip walls as in the Couette case, can be recovered for special relations between some eigenvalues of the collision operator. Despite these results there have still been numerous attempts to set the boundary conditions on the lattice nodes (see, for instance, Refs. [5–9], to name a few). Although most of them have given reasonable results for flat boundary parallel to the main lattice planes, they are not accurate enough when dealing with inclined flat walls or curved ones. To solve this problem we had proposed a different approach based on the reconstruction of the unknown populations from a second-order Chapman-Enskog expansion in Ref. [10]. Recently several authors have proposed various boundary conditions based on a link approach [11–17].

The motivation of the present work is twofold. First we want to emphasize the existence of general theoretical tools to study boundary conditions. Second we extend the results of Ref. [14] in order to derive boundary conditions for gen-

*Present address: Cemagref, DEAN, Groupement Antony, Parc de Tourvoie, BP44, 92163 Antony Cedex, France. Electronic address: irina.ginzburg@cemagref.fr

†Electronic address: dominicq@lps.ens.fr

eral flows, called here “multireflection,” such that the magnitudes of the Knudsen layers are only third-order corrections to the kinetic problem. The analysis of the boundary conditions is done along the lines already introduced in Refs. [2–4]: the boundary condition is written as a closure relation between an unknown population entering the fluid and some others known from the fluid dynamics; the populations are then replaced in the closure relation by their second-order approximations; finally a Taylor expansion of the result at the boundary node gives a second-order estimate of the perturbation of the kinetic solution by the boundary condition. If this estimate is zero, the boundary condition is said to be “third-order kinetic accurate.” For some flows and geometries (for instance Poiseuille flows along the symmetry axis of the lattice), a nonzero estimate can be recast as a shift in the actual location of the walls and the boundary condition does not create Knudsen layers; this is not the case for general flows and the estimate gives the order of magnitude of the Knudsen layer produced by the boundary condition.

Indeed this does not preclude the fact that the bulk solution of the lattice Boltzmann equation is only a second-order approximation of the bulk solution of the Navier-Stokes one. If the physics of the studied flow is dominated by bulk phenomena, third-order kinetic accuracy would probably not be necessary. However, our study has been done in the context of moderate resolutions and/or moving boundaries for which we will show that decreasing the Knudsen effects is very important.

The scope of this work is restricted to boundary conditions involving only populations moving along the same or opposite directions on the same line and on at most three fluid nodes at the same time. Presently the third-order kinetic accuracy of multireflection is proven theoretically and studied numerically for incompressible steady flows. The extension of these results to compressible and/or unsteady flows is left for future work.

In Sec. II we give the general framework for our lattice Boltzmann models and sketch the associated Chapman-Enskog expansion. Section III is devoted to the definition of the boundary conditions considered here and to their theoretical analysis. The results are summarized in Sec. III F. In Sec. IV the standard definition of the momentum exchange between the fluid and a boundary is recalled and a modified definition is proposed to improve the accuracy. Using a 15-velocity model in three dimensions (denoted D3Q15 in Ref. [27]), these boundary conditions have been tested for Stokes flows over a cubic array of spheres in Sec. V A 4, a square array of cylinders in Sec. V A 5, and a periodic line of cylinders between moving walls in Sec. V A 6. Results for Navier-Stokes flows over a square array of cylinders are given in Sec. V B. In Sec. VI we present some possible modifications of the static algorithms to deal with moving boundaries and we test them by simulating a cylinder moving between two parallel flat walls and a sphere moving in a cylinder.

II. LATTICE BOLTZMANN MODELS

A. General models

The lattice Boltzmann models considered here are defined on a cubic lattice in D dimensions by $b = b_m + 1$ velocities

TABLE I. Equilibrium weights t_p and t_p^* .

Model	t_0	t_0^*	$t_1^* = 3t_1$	$t_2^* = 3t_2$	$t_3^* = 3t_3$
$D2Q9$	$\frac{4}{9}$	$\frac{3-5c_s^2}{3c_s^2}$	$\frac{1}{3}$	$\frac{1}{12}$	
$D3Q15$	$\frac{2}{9}$	$\frac{3-7c_s^2}{3c_s^2}$	$\frac{1}{3}$		$\frac{1}{24}$

\vec{c}_i , $i \in \{0, \dots, b_m\}$ (\vec{c}_0 being a zero vector). The velocity set is chosen such that it has the same symmetry group as the cubic lattice; in particular it is invariant under the central symmetry (i.e., if \vec{c}_q is an element of the set, $\vec{c}_q^- = -\vec{c}_q$ is also an element), and the set is invariant by any exchange of coordinates.

These models obey the following evolution equation for the population f_i moving with velocity \vec{c}_i :

$$f_i(\vec{r} + \vec{c}_i, t + 1) = \tilde{f}_i(\vec{r}, t), \quad (1)$$

$$\tilde{f}_i(\vec{r}, t) = f_i(\vec{r}, t) - [\mathbf{A} \cdot \mathbf{f}^{\text{ne}}(\vec{r}, t)]_i + t_p^* \vec{c}_i \cdot \vec{F}, \quad (2)$$

where \mathbf{A} is the collision matrix, the t_p^* are parameters given later [see Eqs. (7) and (8), and Table I], \vec{F} is a body force, and $\mathbf{f}^{\text{ne}} = \mathbf{f} - \mathbf{f}^{\text{eq}}$ [$\mathbf{f} = (f_i)$]. The equilibrium distribution $\mathbf{f}^{\text{eq}} = (f_i^{\text{eq}})$ is a function of the conserved quantities ρ and \vec{J} such that

$$\sum_{i=0}^{b_m} f_i^{\text{eq}} = \sum_{i=0}^{b_m} f_i = \rho, \quad (3)$$

$$\sum_{i=0}^{b_m} f_i^{\text{eq}} c_{i\alpha} = \sum_{i=0}^{b_m} f_i c_{i\alpha} = J_\alpha \quad \forall \alpha. \quad (4)$$

Here and in the sequel, greek subscripts stand for the spatial coordinates, x , y , and so on; in addition repeated greek indices correspond to implicit summations over the space coordinates.

The collision matrix \mathbf{A} is defined by its eigenvectors \mathbf{e}_k and eigenvalues λ_k (in the interval $]0, 2[$ for linear stability):

$$\mathbf{A} \cdot \mathbf{f}^{\text{ne}} = \sum_{k=0}^{b_m} \frac{\lambda_k}{\|\mathbf{e}_k\|^2} (\mathbf{f}^{\text{ne}} \cdot \mathbf{e}_k) \mathbf{e}_k. \quad (5)$$

As in Ref. [18], the eigenvectors \mathbf{e}_k are built from polynomials of the components of the \vec{c}_i which are then orthogonalized. The procedure starts with the $D+1$ b -vectors \mathbf{e}_0 , $(\mathbf{e}_0)_i = 1$, and \mathbf{e}_k , $(\mathbf{e}_k)_i = c_{i\alpha}$ ($k \in \{1, \dots, D\}$). It then proceeds with a b vector \mathbf{e}_{D+1} built on the $c_i^2 = \|\vec{c}_i\|^2$ and orthogonal to \mathbf{e}_0 , $D-1$ pairwise orthogonal vectors built from $Dc_{i\alpha}^2 - c_i^2$, and $D(D-1)/2$ vectors \mathbf{e}_k , $(\mathbf{e}_k)_i = c_{i\alpha} c_{i\beta}$ with

$\alpha \neq \beta$. Note that the preceding vectors have to be all nonzero in order to recover the usual Navier-Stokes equations. The procedure continues with higher degree polynomials and ends when the set of linearly independent orthogonal vectors has been exhausted. This construction is unique if it proceeds by increasing polynomial degrees and decreasing symmetry, i.e., b vectors having in the physical space the symmetry of a scalar, then of a vector, a second rank tensor, and so on. This set of vectors \mathbf{e}_k defines what is usually called the moment basis, the moments being the projections of population distribution \mathbf{f} on them: $m_k = \mathbf{f} \cdot \mathbf{e}_k$. Finally the equilibrium is defined in the moment space as a function of the conserved quantities compatible with the symmetries of the lattice (see Refs. [15,18–21] for details and examples of moment bases).

B. Simplified models

Although the theory for boundary condition can be done in the above general framework, the algebra is simpler when using only two eigenvalues: λ_ν for the vectors \mathbf{e}_k unchanged by central symmetry and λ_2 for the others, and the following equilibrium distribution:

$$f_i^{\text{eq}}(\rho, \vec{J}) = t_p^*(c_s^2 \rho + J_i) + 3t_p \frac{3j_i^2 - j^2}{2\tilde{\rho}}, \quad (6)$$

where $J_i = \vec{J} \cdot \vec{c}_i = J_\alpha c_{i\alpha}$, $j_i = \vec{j} \cdot \vec{c}_i = j_\alpha c_{i\alpha}$, $p = \|\vec{c}_i\|^2$, and $\tilde{\rho}$ is equal to $\rho(\vec{r}, t)$ for the compressible Navier-Stokes equation and to ρ_0 for its incompressible variant (see Refs. [22,23]). The t_p and t_p^* are model dependent and must obey at least the constraints

$$\sum_{i=0}^{b_m} t_p = \sum_{i=0}^{b_m} t_p^* c_s^2 = 1, \quad (7)$$

$$3 \sum_{i=0}^{b_m} t_p c_{i\alpha} c_{i\beta} = \sum_{i=0}^{b_m} t_p^* c_{i\alpha} c_{i\beta} = \delta_{\alpha\beta} \quad \forall \alpha, \beta, \quad (8)$$

coming from the conservation laws (3) and (4). The momentum \vec{J} used in the nonlinear term of Eq. (6) is defined as

$$\vec{J} = \vec{J} - I_t \vec{F}, \quad (9)$$

where $I_t = 0$ for the standard definition and $I_t = -1/2$ for the modified one which is used here (see Refs. [3,24–26]). The “incompressible” variant with $\tilde{\rho} = \rho_0$ has also been used for all the steady simulations presented here.

The parameters t_p and t_p^* are given for the $D2Q9$ and $D3Q15$ models in Table I (note that the t_p are those given in Refs. [27,28] and the t_p^* are defined to keep the speed of sound as a free parameter). With these choices the nonlinear terms and the viscosity are isotropic and the viscosity is given by

$$\nu = \frac{1}{3} \left(\frac{1}{\lambda_\nu} - \frac{1}{2} \right) = \frac{2\tau - 1}{6}, \quad (10)$$

with $\tau = 1/\lambda_\nu$.

In the simulations reported in Sec. V A, we use the following equilibrium:

$$f_i^{\text{eq}}(\rho, \vec{J}) = t_p^*(c_s^2 \rho + J_i), \quad (11)$$

which leads to the Stokes equation which is written for stationary incompressible case as

$$\vec{\nabla} P - \vec{F} = \nu \Delta \vec{J}, \quad \vec{\nabla} \cdot \vec{j} = 0, \quad P = c_s^2 \rho. \quad (12)$$

C. Simplified Chapman-Enskog expansion

Neglecting the third-order and higher derivatives of the momentum and the second-order and higher derivatives of the density and of the nonlinear terms, the populations can be approximated as

$$f_i \approx f_i^{\text{eq}} + f_i^{(1)} + f_i^{(2)}, \quad (13)$$

where $f_i^{(1)}$ is related to the first-order derivatives of the momentum through some second-order tensor $E_{i\alpha\beta}^{(2)}$ by

$$f_i^{(1)} = -\frac{1}{\lambda_\nu} \partial_{\beta j} j_\alpha E_{i\alpha\beta}^{(2)}, \quad (14)$$

and $f_i^{(2)}$ is related to the second-order derivatives of the momentum and the first-order derivatives of the nonlinear terms through some third-order tensor $E_{i\alpha\beta\gamma}^{(3)}$ by

$$f_i^{(2)} = \frac{1}{\lambda_2} \left(\nu \partial_{\beta\gamma} j_\alpha - \partial_\gamma \frac{j_\alpha j_\beta}{2\tilde{\rho}} \right) E_{i\alpha\beta\gamma}^{(3)}. \quad (15)$$

The projections of the tensors $E_{i\alpha\beta}^{(2)}$ and $E_{i\alpha\beta\gamma}^{(3)}$ on the first $D+1$ vectors \mathbf{e}_k must be equal to zero due to the conservation laws (3) and (4). Since $\partial_{\beta j} j_\alpha$ is unchanged by a central symmetry while $\partial_{\beta\gamma} j_\alpha$ and $\partial_\gamma (j_\alpha j_\beta / (2\tilde{\rho}))$ change their signs, it comes

$$(\mathbf{A} \cdot \mathbf{f}^{\text{ne}})_i = \lambda_\nu f_i^{(1)} + \lambda_2 f_i^{(2)}. \quad (16)$$

Taking the value of the terms in Eq. (13) at (\vec{r}, t) and $(\vec{r} + \vec{c}_i, t+1)$, the Taylor expansion of the difference $f_i(\vec{r} + \vec{c}_i, t+1) - f_i(\vec{r}, t)$ must be equal to the corresponding expansion of $-(\mathbf{A} \cdot \mathbf{f}^{\text{ne}})_i + t_p^* \vec{c}_i \cdot \vec{F}$. After some tedious but straightforward algebra, one gets

$$E_{i\alpha\beta}^{(2)} = t_p^*(c_{i\alpha} c_{i\beta} - c_s^2 \delta_{\alpha\beta}), \quad (17)$$

$$E_{i\alpha\beta\gamma}^{(3)} = t_p^*(3c_{i\alpha} c_{i\beta} c_{i\gamma} - c_{i\alpha} \delta_{\beta\gamma} - c_{i\beta} \delta_{\alpha\gamma} - c_{i\gamma} \delta_{\alpha\beta}). \quad (18)$$

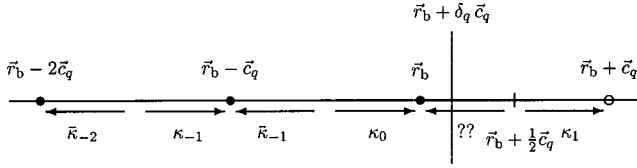


FIG. 1. A boundary surface cutting at $\vec{r}_b + \delta_q \vec{c}_q$ the link between fluid node \vec{r}_b and an outside one at $\vec{r}_b + \vec{c}_q$. The solid circles represent the fluid nodes and the open circle represents an outside node.

The tensors $E_{i\alpha\beta}^{(2)}$ and $E_{i\alpha\beta\gamma}^{(3)}$ are unchanged by any permutation of their greek subscripts. In general, their components are linear combinations of the components of the \mathbf{e}_k 's introduced in Sec. II A. For the $D2Q9$ and $D3Q15$ models considered here, most of the components $E_{i\alpha\beta}^{(2)}$ and $E_{i\alpha\beta\gamma}^{(3)}$ are equal to components of some \mathbf{e}_k , except for the $E_{i\alpha\alpha}^{(2)}$. Writing

$$E_{i\alpha\alpha}^{(2)} = t_p^* \left[\left(c_{i\alpha}^2 - \frac{c_i^2}{D} \right) + \left(\frac{c_i^2}{D} - c_s^2 \right) \right], \quad (19)$$

the $E_{i\alpha\alpha}^{(2)}$ are linear combinations of the moments built on $Dc_{i\alpha}^2 - c_i^2$ and of $c_i^2 - Dc_s^2$. The latter components can be expressed in turn as linear combinations, depending on c_s^2 , of the \mathbf{e}_k 's built on c_i^2 and c_i^4 .

For the models such that $c_{i\alpha}^3 = c_{i\alpha}$, the diagonal elements of $E_{i\alpha\beta\gamma}^{(3)}$ are zero: $E_{i\alpha\alpha\alpha}^{(3)} = 0$. For the $D2Q9$ model, $E_{ixyy}^{(3)}$ and $E_{iyxx}^{(3)}$ are, up to a multiplicative constant, the components of the two ‘‘cubic’’ \mathbf{e}_k 's. For the $D3Q15$ model, $E_{ixyy}^{(3)} = E_{ixzz}^{(3)}$ and $E_{ixyz}^{(3)} \neq 0$; with their independent permutations of x , y , and z , they are, up to a multiplicative constant, the components of the four cubic \mathbf{e}_k 's.

III. SIX-POPULATION BOUNDARY CONDITIONS

A. Definitions

The boundary conditions presented here are based on the following definitions.

(1) *Fluid nodes* are defined as the nodes \vec{r} such that (a) the collision step is given by Eq. (2) without any change; (b) the propagation step between them is given by Eq. (1). The set of fluid nodes is denoted \mathcal{F} . The nodes that are not in \mathcal{F} are considered as ‘‘outside’’ nodes.

(2) A *boundary node* $\vec{r}_b \in \mathcal{B}$ is defined as a fluid node having at least one neighbor $\vec{r}_b + \vec{c}_q$ (where $\vec{c}_q \in \{\vec{c}_i\}$) which is not a fluid node. The set of boundary nodes and the set of cut links (connecting a boundary node to an outside one) are denoted \mathcal{B} and \mathcal{C} , respectively.

(3) The boundary conditions are given on a $(D-1)$ -surface Ω which intersects the link between \vec{r}_b and $\vec{r}_b + \vec{c}_q$ at $\vec{r}_b + \delta_q \vec{c}_q$ (see Fig. 1). We here consider only Dirichlet boundary conditions corresponding to a given velocity $\vec{u}_w(\vec{r}_b + \delta_q \vec{c}_q, t+1)$ on Ω . The associated momentum \vec{J}_w is defined by

$$\vec{J}_w = \tilde{\rho}_b \vec{u}_w, \quad (20)$$

where $\tilde{\rho}_b$ is equal to $\rho(\vec{r}_b, t)$ for the compressible Navier-Stokes and to ρ_0 for its incompressible variant [22,23], according to the choice made for Eq. (6).

After the propagation step at t , the postcollision population $\tilde{f}_q(\vec{r}_b, t)$ has left the fluid and can be thought to be on the outside node $\vec{r}_b + \vec{c}_q$ as $f_q(\vec{r}_b + \vec{c}_q, t+1)$. At the same time the population $f_q^-(\vec{r}_b, t+1)$, corresponding to the direction $\vec{c}_q^- = -\vec{c}_q$, is unknown and has to be supplied by the boundary condition. In the sequel we will restrict our attention to the following closure relation:

$$\begin{aligned} f_q^-(\vec{r}_b, t+1) = & \kappa_1 f_q(\vec{r}_b + \vec{c}_q, t+1) + \kappa_0 f_q(\vec{r}_b, t+1) \\ & + \kappa_{-1} f_q(\vec{r}_b - \vec{c}_q, t+1) + \bar{\kappa}_{-1} f_q^-(\vec{r}_b - \vec{c}_q, t+1) \\ & + \bar{\kappa}_{-2} f_q^-(\vec{r}_b - 2\vec{c}_q, t+1) - w_q t_p^* j_{qw} + t_p^* F_q^{\text{pc}}, \end{aligned} \quad (21)$$

where the symbols with an overbar refer to quantities associated with \vec{c}_q^- . The coefficients κ_1 , κ_0 , $\bar{\kappa}_{-1}$, κ_{-1} , $\bar{\kappa}_{-2}$ are referred to as the coefficients of the interpolations or of the multireflection boundary condition. The term $w_q t_p^* j_{qw}$ is used to set the Dirichlet boundary condition ($j_{qw} = \vec{J}_w \cdot \vec{c}_q$). The term F_q^{pc} is discussed in Sec. III E.

Using Eq. (1), relation (21) can also be written in terms of the postcollision distributions, either for some terms or for all of them, as in

$$\begin{aligned} f_q^-(\vec{r}_b, t+1) = & \kappa_1 \tilde{f}_q(\vec{r}_b, t) + \kappa_0 \tilde{f}_q(\vec{r}_b - \vec{c}_q, t) \\ & + \kappa_{-1} \tilde{f}_q(\vec{r}_b - 2\vec{c}_q, t) + \bar{\kappa}_{-1} \tilde{f}_q^-(\vec{r}_b, t) \\ & + \bar{\kappa}_{-2} \tilde{f}_q^-(\vec{r}_b - \vec{c}_q, t) - w_q t_p^* j_{qw} + t_p^* F_q^{\text{pc}}. \end{aligned} \quad (22)$$

The choice between Eq. (21) and Eq. (22) is mostly a matter of taste. Equations (29) and (31) below have been obtained with Eq. (22); using Eq. (21) instead leads to the same final results for steady flows, but with different intermediate steps.

The above boundary condition has the following properties. First, with $F_q^{\text{pc}} = 0$, it is a generalization of the bounce-back rule (with the Dirichlet condition) and of the linear and quadratic interpolations introduced in Ref. [14]: bounce back corresponds to

$$\kappa_1 = 1, \quad w_q = 2, \quad \text{and} \quad \kappa_0 = \kappa_{-1} = \bar{\kappa}_{-1} = \bar{\kappa}_{-2} = 0; \quad (23)$$

the upwind linear interpolation for $0 \leq \delta_q \leq 1/2$ corresponds to

$$\begin{aligned} \kappa_1 = 2\delta_q, \quad \kappa_0 = 1 - 2\delta_q, \quad w_q = 2, \\ \text{and} \quad \kappa_{-1} = \bar{\kappa}_{-1} = \bar{\kappa}_{-2} = 0; \end{aligned} \quad (24)$$

and the downwind linear interpolation for $1/2 \leq \delta_q$ corresponds to

$$\kappa_1 = \frac{1}{2\delta_q}, \quad \bar{\kappa}_{-1} = \frac{2\delta_q - 1}{2\delta_q}, \quad w_q = \frac{1}{\delta_q},$$

and $\kappa_0 = \kappa_{-1} = \bar{\kappa}_{-2} = 0$. (25)

Note also that Eqs. (33)–(36) of Ref. [17] give

$$\kappa_1 = \frac{\delta_q}{1 + \delta_q}, \quad \kappa_0 = \frac{1 - \delta_q}{1 + \delta_q}, \quad \bar{\kappa}_{-1} = \frac{\delta_q}{1 + \delta_q},$$

$$w_q = \frac{2}{1 + \delta_q}, \quad \text{and} \quad \kappa_{-1} = \bar{\kappa}_{-2} = 0. \quad (26)$$

The upwind (downwind) quadratic interpolations in Ref. [14] correspond to $\bar{\kappa}_{-1} = \bar{\kappa}_{-2} = 0$ ($\kappa_0 = \kappa_{-1} = 0$), the other coefficients being given in their Eq. (6a) [Eq. (6b), their q being replaced by our δ_q].

Second relations (21) and (22) involve only the populations considered in Ref. [14].

Finally all the required information is available at the boundary node \vec{r}_b and its fluid neighbor $\vec{r}_b - \vec{c}_q$, using their four postcollision distributions at time t , see Eq. (22), and $f_q(\vec{r}_b - \vec{c}_q, t + 1)$ after the propagation step. This property is quite important for parallel codes in which the communications are restricted to the nearest neighbors along $\pm \vec{c}_q$. Equation (22) requires three fluid nodes along the link in order to be used as such. When there are only two fluid nodes available, the equation can be modified in several ways. The simplest one, used here, consists in replacing $f_q(\vec{r}_b - \vec{c}_q, t + 1)$ by $f_q(\vec{r}_b - \vec{c}_q, t)$ in relation (21). A second one applies when the boundary for $\vec{r}_b - 2\vec{c}_q$ is a flat wall located at $\delta_q = 1/2$; in this case the bounce-back condition is applied first and its result provides the missing population.

Note that the boundary conditions (21) or (22) do not in general enforce the conservation of the mass defined for all fluid cells in Eq. (3). This has to be contrasted to the boundary conditions of Refs. [12] and [16].

B. Closure relation

In the sequel we use the following notations: $j_q = \vec{J} \cdot \vec{c}_q$ and $F_q = \vec{F} \cdot \vec{c}_q$ are the projections of \vec{J} and \vec{F} on \vec{c}_q ; ∂_q and ∂_{qq} are the first and second derivatives along \vec{c}_q ($\partial_q = c_{q\alpha} \partial_\alpha$). With these notations and with relations (17) and (18), the first- and second-order nonequilibrium terms (14) and (15) become, respectively,

$$f_q^{(1)} = -t_p^* \frac{1}{\lambda_\nu} (\partial_q j_q - c_s^2 \vec{\nabla} \cdot \vec{j}), \quad (27)$$

$$f_q^{(2)} = t_p^* \frac{1}{\lambda_2} \left(\nu (3\partial_{qq} j_q - \Delta j_q - 2\partial_q \vec{\nabla} \cdot \vec{j}) - \partial_q \frac{3j_q^2 - j^2}{2\tilde{\rho}} + \partial_\alpha \frac{j_\alpha j_q}{\tilde{\rho}} \right). \quad (28)$$

The closure relation (22) is then analyzed by replacing the distributions f_q and f_q^- (or \tilde{f}_q and \tilde{f}_q^-) by their second-order Chapman-Enskog expansion. This first step is followed by a Taylor expansion of the conserved quantities around their values at \vec{r}_b (see Appendix A). For incompressible flows $\vec{\nabla} \cdot \vec{j} = 0$, relation (22) leads to

$$A_0 j_q + A_1 \partial_q j_q + A_2 \partial_{qq} j_q + F_q^{\text{pc}} + (A_p - 1) \left(P + \frac{3j_q^2 - j^2}{2\tilde{\rho}} \right) + A_\nu \left(\nu \Delta j_q + \partial_q \frac{3j_q^2 - j^2}{2\tilde{\rho}} - \partial_\alpha \frac{j_\alpha j_q}{\tilde{\rho}} \right) + A_p' \partial_q \left(P + \frac{3j_q^2 - j^2}{2\tilde{\rho}} \right) + A_F F_q = w_q j_{q\text{w}} + O(\vec{\nabla} \cdot \vec{j}) + O(\epsilon^3), \quad (29)$$

with

$$A_p = \kappa_1 + \kappa_0 + \bar{\kappa}_{-1} + \kappa_{-1} + \bar{\kappa}_{-2} = 1, \quad (30)$$

$$A_0 = 2 - 2(\bar{\kappa}_{-1} + \bar{\kappa}_{-2}),$$

$$A_1 = 1 - (\kappa_0 + 2\kappa_{-1} + \bar{\kappa}_{-2}),$$

$$A_F = 1 - 2(\bar{\kappa}_{-1} + \bar{\kappa}_{-2}) + 2I_{\text{fl}} [1 - (\bar{\kappa}_{-1} + \bar{\kappa}_{-2})],$$

$$A_p' = -(\kappa_0 + 2\kappa_{-1} + \bar{\kappa}_{-2}),$$

$$A_2 = -3\nu A_\nu + A_j + A_{j'},$$

$$A_\nu = - \left[\frac{1}{\lambda_2} + \left(\frac{1}{\lambda_2} - 1 \right) [1 - 2(\bar{\kappa}_{-1} + \bar{\kappa}_{-2})] \right],$$

$$A_j = \left(\frac{\kappa_0}{2} + 2\kappa_{-1} - \frac{\bar{\kappa}_{-2}}{2} \right),$$

$$A_{j'} = \left(\frac{1}{\lambda_\nu} - 1 \right) (\kappa_0 + 2\kappa_{-1} + \bar{\kappa}_{-2}), \quad (31)$$

where the term κ_1 has been removed from A_0 to $A_{j'}$, using $A_p = 1$, a condition required to remove the pressure (density) term from the closure relation (29) and which is always as-

sumed to be satisfied in what follows. Note that the nonlinear terms disappear when the linear equilibrium (11) is used; then Eq. (29) is obviously verified for the linear equilibrium if the flow and the forcing are perpendicular to \vec{c}_q ($j_q = j_{qw} = F_q = 0$), $\partial_q P = 0$, and $F_q^{\text{pc}} = 0$.

Note that the closure relation (29) applies also to the boundary conditions of Refs. [11] and [13] by replacing F_q^{pc} by the equilibrium population computed at the solid node.

C. Couette flow

Let us first consider the flow between two parallel planes moving with parallel but different velocities in the absence of body force ($F_q = 0$). The corresponding steady flow, called Couette flow, is a pure shear flow for which the density is uniform and only the first-order spatial derivatives are nonzero (uniform shear). Taking $F_q^{\text{pc}} = 0$ and the linear equilibrium (11), Eq. (29) becomes

$$A_0 j_q + A_1 \partial_q j_q = w_q j_{qw}. \quad (32)$$

Then the Dirichlet boundary condition j_{qw} is met at $\vec{r}_b + \delta_q \vec{c}_q$ when the following conditions are satisfied:

$$\frac{A_1}{A_0} = \delta_q, \quad (33)$$

$$w_q = A_0. \quad (34)$$

Using Eqs. (30), (33), and (34) the coefficients κ_1 , κ_0 , and w_q must be related to the other ones by

$$\kappa_1 = 2\delta_q + \kappa_{-1} - (1 + 2\delta_q)\bar{\kappa}_{-1} - (2 + 2\delta_q)\bar{\kappa}_{-2}, \quad (35)$$

$$\kappa_0 = 1 - 2\delta_q - 2\kappa_{-1} + 2\delta_q\bar{\kappa}_{-1} + (1 + 2\delta_q)\bar{\kappa}_{-2}, \quad (36)$$

$$w_q = 2(1 - \bar{\kappa}_{-1} - \bar{\kappa}_{-2}). \quad (37)$$

For the bounce-back coefficients (23) these conditions are satisfied only if $\delta_q = 1/2$. This is possible only when the moving planes are parallel to the symmetry planes of the underlying lattice, for which the links are either perpendicular to the velocity or cut midway through the boundary nodes and the nearest outside ones. For these special orientations of the moving planes, the solution of the linear LB equation with bounce back is exact (up to machine accuracy) if the planes are located at $\delta_q = 1/2$ (as found in Ref. [2]); note that this exact solution is lost and the apparent convergence rate is only first-order in the grid resolution if the planes are mistakenly located on the boundary nodes or on the nearest outside ones. For the other orientations of the moving planes, the bounce-back rule is no longer compatible with Couette flows. Since for these orientations δ_q takes values between 0 and 1, one expects a first-order convergence rate with the grid resolution.

When the multireflection coefficients are chosen such that relations (35)–(37) hold for all the boundary nodes and links, the Couette flow is an exact solution of the linear LB equation with the corresponding boundary conditions for any orientation of the moving planes and any distances between them. It is easy to check that this is the case for the linear interpolations (24) and (25).

At this point it is important to realize that relations (35)–(37) are necessary conditions for any order (≥ 1) boundary conditions and apply implicitly in the following sections.

D. Poiseuille-Hagen flow between parallel plates

Let us now consider the flow between two parallel plane walls, at rest and symmetric with respect to the origin, and due to uniform forcing \vec{F} parallel to the walls. Along any line parallel to \vec{c}_q , the coordinates x_q (or any length) are defined using \vec{c}_q as unit vector and the middle of the fluid segment as the origin. Then the planes intersect the line at $\pm(x_{qb} + \delta_q)$ and the exact solution of the linear LB equation is a parabolic flow given by

$$j_q = j_{0q} \left(1 - \frac{4x_q^2}{H_{q\text{eff}}^2} \right), \quad (38)$$

where $H_{q\text{eff}}$ is an effective width depending on the boundary condition. Denoting Θ_q the projection of \vec{c}_q on the direction perpendicular to the walls (in lattice unit), since $\partial_q P = 0$ and $\partial_{qq} j_q = \Theta_q^2 \Delta j_q$ for Poiseuille flows, j_{0q} is related to F_q , Θ_q , $H_{q\text{eff}}$, and ν by

$$F_q = j_{0q} \frac{8\nu}{\Theta_q^2 H_{q\text{eff}}^2}. \quad (39)$$

Taking $F_q^{\text{pc}} = 0$ and using Eq. (10) and Eqs. (35)–(38) and neglecting the nonlinear terms [linear equilibrium (11)], Eq. (29) leads to the following relation between $H_{q\text{eff}}$ and $H_q = 2(x_{qb} + \delta_q)$, the prescribed width along \vec{c}_q :

$$\begin{aligned} H_{q\text{eff}}^2 = & H_q^2 + 6\Lambda^2 - 4\delta_q^2 - \frac{8\nu}{\Theta_q^2} \left(\frac{1}{\lambda_2} + I_f \right) + \frac{4(\kappa_{-1} - \bar{\kappa}_{-2})}{1 - \bar{\kappa}_{-1} - \bar{\kappa}_{-2}} \\ & + \frac{12\nu}{1 - \bar{\kappa}_{-1} - \bar{\kappa}_{-2}} [1 - 2\delta_q + (1 + 2\delta_q)\bar{\kappa}_{-1} \\ & + (3 + 2\delta_q)\bar{\kappa}_{-2}], \end{aligned} \quad (40)$$

where

$$\Lambda^2 = \frac{4}{3} \left(\frac{1}{\lambda_\nu} - \frac{1}{2} \right) \left(\frac{1}{\lambda_2} - \frac{1}{2} \right). \quad (41)$$

For a forcing along one of the main axes (x , y , etc.), either $j_q = 0$ (and the closure relation is verified) or $\Theta_q^2 = 1$ and Eq. (40) relates the effective width of the parabolic profile to its

prescribed value. For the bounce-back rule [$\delta_q=1/2$ and the coefficients given in Eq. (23)] and $I_f=-1/2$, Eq. (40) becomes

$$D_{\text{eff}}^2 = D_{1/2}^2 + 4\Lambda^2 - 1, \quad (42)$$

where D_{eff} is the effective diameter and $D_{1/2}$ is the diameter based on the middle of the cut links. For $\Lambda^2=1/4$ or

$$\lambda_2(\lambda_\nu) = 8 \frac{2 - \lambda_\nu}{8 - \lambda_\nu}, \quad (43)$$

the Poiseuille profile is the exact Poiseuille solution found in [3,4] for walls located at $\pm(x_{qb}+1/2)$, as for Couette flows. Note that for Bhatnagar-Gross-Krook (BGK) models ($\lambda_2 = \lambda_\nu$), [45] $\Lambda^2 = 12\nu^2$ and the walls are located exactly at $\pm(x_{qb}+1/2)$ for $\nu=1/\sqrt{48}$. When $\Lambda^2 \neq 1/4$, the relative error made by taking $D_{1/2}$ instead of D_{eff} is approximately $(4\Lambda^2 - 1)/(2D_{1/2}^2)$. Then locating the walls on the middle of the cut links is second-order accurate, however the prefactor $4\Lambda^2 - 1$ can be large for large values of Λ^2 . For the BGK case, the prefactor is $48\nu^2 - 1$ and increases very rapidly with the viscosity: for instance, if $D_{1/2}=10$ lattice units and $\nu=1$ ($\tau=7/2$), $D_{\text{eff}} \approx 12.1$, i.e., the relative error is larger than 20% (for $\tau=50$, the effective width is larger than 11 times the prescribed one, see, for instance, Fig. 2 in Ref. [7]).

A very important property of the bounce-back condition for the measurements reported in Sec. V A is that the permeability is independent of the viscosity if the coefficient Λ^2 is kept constant, even for arbitrary complex flows. For each particular flow, the precision can be further improved for an appropriate choice of Λ^2 [29] (a good starting value being in general close to $1/4$). So far we have been unable to prove theoretically this property; however, this is strongly confirmed by all our numerical simulations (see Sec. V A 3).

For the interpolations of Ref. [14] and $\Theta_q^2=1$, Eq. (42) gives the error in the wall location as a function of ν , Λ^2 , δ_q^2 and I_f . It is again possible to choose λ_2 as a function of λ_ν to set this error to zero, but this is no longer possible for a fixed value of Λ^2 . For arbitrary inclined Poiseuille flows, the errors cannot be canceled for all the values of δ_q for constant values of λ_ν , λ_2 , and I_f . As a consequence, none of the interpolations of Ref. [14] give exact parabolic profiles for arbitrary inclined Poiseuille flows.

By setting two coefficients in the set $\{\kappa_0, \kappa_{-1}, \bar{\kappa}_{-1}, \bar{\kappa}_{-2}\}$ to zero, we have been able to derive six sets of relations, for κ_1 and the two other coefficients, giving exact inclined Poiseuille flows. In addition these sets are independent of Θ_q for $I_f = -1/\lambda_2$. However, we did not succeed in finding rules to choose among them as a function of δ_q in order to guarantee numerical stability. In addition, these results are superseded by the results of the following section.

E. General flows

For general flows, the relation between Δj_q and $\partial_{qq} j_q$ is not known *a priori* and the Dirichlet boundary condition, exact up to second order,

$$j_{qw}(\vec{r}_b + \delta_q \vec{c}_q) = j_q(\vec{r}_b + \delta_q \vec{c}_q) \\ = (j_q + \delta_q \partial_q j_q + \frac{1}{2} \delta_q^2 \partial_{qq} j_q)(\vec{r}_b), \quad (44)$$

cannot be obtained from Eq. (29) if $F_q^{\text{pc}}=0$. However, Eqs. (29) and (44) match when the following relations are verified (sufficient conditions):

$$A_F = 0, \quad A'_p = 0, \quad w_q = A_0,$$

$$\frac{A_1}{A_0} = \delta_q, \quad \frac{A_2 + 3\nu A_\nu}{A_0} = \frac{1}{2} \delta_q^2,$$

$$F_q^{\text{pc}} = A_\nu \left(\nu(3\partial_{qq} j_q - \Delta j_q) - \partial_q \frac{3j_q^2 - j^2}{2\tilde{\rho}} + \partial_\alpha \frac{j_\alpha j_q}{\tilde{\rho}} \right) \\ = \frac{A_\nu \lambda_2}{t_p^*} f_q^{(2)}, \quad (45)$$

where the last right hand side term comes from Eq. (28).

The conditions $I_f = -1/2$ and $A_F = 0$ imply $A_0 = 2$, $\bar{\kappa}_{-1} = -\bar{\kappa}_{-2}$, $\nu A_\nu = -\Lambda^2/2$, and

$$t_p^* F_q^{\text{pc}} = \frac{\Lambda^2}{2\nu} \tilde{f}_q^{(2)} = -\frac{\Lambda^2}{2\nu} \lambda_2 f_q^{(2)}. \quad (46)$$

From a technical point of view, $\tilde{f}_q^{(2)}$ is computed from the part of the sum in Eq. (5) restricted to the \mathbf{e}_k built from the third-order polynomials (the nonzero $E_{i\alpha\beta\gamma}^{(3)}$ in Sec. II C).

The conditions $I_f = -1/2$ and (45) lead to

$$\kappa_1 = 2\delta_q + \delta_q^2,$$

$$\kappa_0 = \frac{3}{2} - 3\delta_q - 2\delta_q^2,$$

$$\kappa_{-1} = -\frac{1}{2} + \delta_q + \delta_q^2,$$

$$\bar{\kappa}_{-1} = \frac{1}{2} - \delta_q,$$

$$\bar{\kappa}_{-2} = -\frac{1}{2} + \delta_q,$$

$$w_q = 2. \quad (47)$$

It is easy to check that $0 \leq \kappa_1 \leq 3$, $-7/2 \leq \kappa_0 \leq 3/2$, and $-1/2 \leq \kappa_{-1} \leq 3/2$ for $0 \leq \delta_q \leq 1$, i.e., these coefficients have values outside the interval $[-1, 1]$ for some values of δ_q . Although we do not have solid stability analysis for the boundary conditions, we have found numerically that values outside $[-1, 1]$ very often lead to numerical instabilities.

Noticing that the macroscopic closure relation (29) is not changed, at least up to third order, under the following transformation:

$$\begin{aligned}\kappa_1 &\rightarrow (\kappa_1 - \kappa)/(\kappa + 1), & \kappa_0 &\rightarrow (\kappa_0 + 2\kappa)/(\kappa + 1) \\ \kappa_{-1} &\rightarrow (\kappa_{-1} - \kappa)/(\kappa + 1), & \bar{\kappa}_{-1} &\rightarrow (\bar{\kappa}_{-1} + 2\kappa)/(\kappa + 1), \\ \bar{\kappa}_{-2} &\rightarrow (\bar{\kappa}_{-2} - \kappa)/(\kappa + 1), \\ w_q &\rightarrow w_q/(\kappa + 1), & F_q^{\text{pc}} &\rightarrow F_q^{\text{pc}}/(\kappa + 1),\end{aligned}\quad (48)$$

where κ is an arbitrary constant, a one-parameter family of coefficient can be constructed. In order to show this result, one has to use the projected stationary Navier-Stokes equation:

$$\partial_\alpha \frac{j_\alpha j_q}{\bar{\rho}} + \partial_q P = F_q + \nu \Delta j_q. \quad (49)$$

For instance, taking

$$\kappa = -\frac{1}{2}(1 - 2\delta_q - \delta_q^2) \quad (50)$$

leads to a new set of coefficients

$$\begin{aligned}\kappa_1 &= 1, \\ \kappa_0 = -\bar{\kappa}_{-1} &= \frac{1 - 2\delta_q - 2\delta_q^2}{(1 + \delta_q)^2}, \\ \kappa_{-1} = -\bar{\kappa}_{-2} &= \frac{\delta_q^2}{(1 + \delta_q)^2}, \\ w_q &= \frac{4}{(1 + \delta_q)^2},\end{aligned}\quad (51)$$

which stay in the interval $[-1, 1]$ for $0 \leq \delta_q \leq 1$. This set of coefficients share some properties of the bounce-back condition. On the positive side the higher-order errors (hence the permeability) are found independent of the viscosity for fixed values of Λ^2 . On the negative side the corresponding boundary condition for the staggered invariants is a free-slip condition, i.e., the staggered invariants are not damped by the boundary when they appear. As for bounce back [30], this effect can be killed by using $f_q(\vec{r}_b + \vec{c}_q, t)$ instead of $f_q(\vec{r}_b + \vec{c}_q, t + 1)$ in Eq. (21).

A probably better way to avoid staggered invariants is to derive an other set of coefficients with $\kappa_1 \neq 1$ for $\delta_q > 0$ and the following constraints:

$$0 \leq \kappa_1 \leq 1 \quad \text{and} \quad \{\kappa_0, \kappa_{-1}, \bar{\kappa}_{-1}, \bar{\kappa}_{-2}\} \in [-1, 1],$$

$$\text{for } 0 \leq \delta_q \leq 1. \quad (52)$$

Choosing the parameter $\kappa^* = 2 - \kappa_0$ and introducing the following polynomials of δ_q :

$$\begin{aligned}\kappa_t &= 3 + 2\delta_q, \\ \kappa_s &= 1 + 6\delta_q + 4\delta_q^2, \\ \kappa_f &= (\kappa_t + \kappa_s)/2 = 2(1 + \delta_q)^2,\end{aligned}\quad (53)$$

the family of coefficients derived from Eq. (47) with transformation (48) can be written as

$$\kappa_1 = \frac{\kappa^* \kappa_f}{\kappa_s} - 1,$$

$$\kappa_0 = 2 - \kappa^*,$$

$$\kappa_{-1} = (\kappa_f - \kappa_t + 2) \frac{\kappa^*}{\kappa_s} - 1,$$

$$\bar{\kappa}_{-1} = 2 - \frac{\kappa^* \kappa_t}{\kappa_s},$$

$$\bar{\kappa}_{-2} = (\kappa_t - 2) \frac{\kappa^*}{\kappa_s} - 1,$$

$$w_q = \frac{4\kappa^*}{\kappa_s}. \quad (54)$$

Constraints (52) are satisfied provided that

$$\max\left\{1, \frac{\kappa_s}{\kappa_t}\right\} \leq \kappa^* \leq \frac{2\kappa_s}{\kappa_f}. \quad (55)$$

The upper bound corresponds to solution (51). The lower bound is 1 for $0 \leq \delta_q \leq \delta_0$ ($\kappa_0 = 1$) and κ_s/κ_t for $\delta_0 \leq \delta_q \leq 1$ ($\bar{\kappa}_{-1} = 1$), with $\delta_0 = (\sqrt{3} - 1)/2$ (when $\delta_q = \delta_0$, $\kappa_f = \kappa_t = \kappa_s$).

For $\delta_q = 0$ the interval reduces to $\kappa^* = 1$ and $\kappa_1 = \kappa_0 = 1$, $\bar{\kappa}_{-1} = -1$, and $\kappa_{-1} = \bar{\kappa}_{-2} = 0$. For $\delta_q = 1$, $\kappa^* \in [11/5, 11/4]$ and κ_0 reach a maximal value $\kappa_{0m} = -1/5$ for $\kappa^* = 11/5$ ($\kappa_1 = 3/5$, $\kappa_{-1} = 0$, $\bar{\kappa}_{-1} = 1$, and $\bar{\kappa}_{-2} = -2/5$).

When $\delta_q = \delta_0$, interval (55) is $[1, 2]$ and is the largest available. $\kappa^* = 1$ gives $\kappa_1 = 0$, $\kappa_0 = \bar{\kappa}_{-1} = 1$, $\kappa_{-1} = 3 - 2\sqrt{3}$, and $\bar{\kappa}_{-2} = 2(\sqrt{3} - 2)$; $\kappa^* = 3/2$ gives $\kappa_1 = \kappa_0 = \bar{\kappa}_{-1} = 1/2$, $\kappa_{-1} = 5 - 3\sqrt{3}$, and $\bar{\kappa}_{-2} = (6\sqrt{3} - 11)/2$; and $\kappa^* = 2$ gives $\kappa_1 = 1$, $\kappa_0 = \bar{\kappa}_{-1} = 0$, and $\kappa_{-1} = -\bar{\kappa}_{-2} = 7 - 4\sqrt{3}$.

Among the infinite set of functions $\kappa^*(\delta_q)$ that satisfy (55), we have chosen to use in Sec. V B

TABLE II. Valid range for δ_q , coefficients κ_1 , κ_0 , κ_{-1} , $\bar{\kappa}_{-1}$, $\bar{\kappa}_{-2}$, w_q , and F_q^{pc} for the different boundary conditions: bounce back (BB); upwind and downwind linear interpolation (ULI and DLI); upwind and downwind quadratic interpolation (UQI and DQI); multireflection (MR).

	BB	ULI	DLI	UQI	DQI	MR
δ_q	$\frac{1}{2}$	$[0, \frac{1}{2}]$	$[\frac{1}{2}, +\infty[$	$[0, \frac{1}{2}]$	$[\frac{1}{2}, 1[$	$[0, 1]$
κ_1	1	$2\delta_q$	$\frac{1}{2\delta_q}$	$\delta_q(1+2\delta_q^2)$	$\frac{1}{\delta_q(2\delta_q+1)}$	$\frac{\kappa^*\kappa_f}{\kappa_s} - 1$
κ_0	0	$1-2\delta_q$	0	$1-4\delta_q^2$	0	$2-\kappa^*$
κ_{-1}	0	0	0	$-\delta_q(1-2\delta_q)$	0	$\kappa_1 - \bar{\kappa}_{-2} - 1$
$\bar{\kappa}_{-1}$	0	0	$\frac{2\delta_q-1}{2\delta_q}$	0	$\frac{2\delta_q-1}{\delta_q}$	$2 - \frac{\kappa^*\kappa_t}{\kappa_s}$
$\bar{\kappa}_{-2}$	0	0	0	0	$-\frac{2\delta_q-1}{1+2\delta_q}$	$\frac{\kappa^*(\kappa_t-2)}{\kappa_s} - 1$
w_q	2	2	$\frac{1}{\delta_q}$	2	$\frac{2}{\delta_q(2\delta_q+1)}$	$\frac{4\kappa^*}{\kappa_s}$
F_q^{pc}	0	0	0	0	0	$\frac{\kappa^*\Lambda^2\tilde{f}_q^{(2)}}{t_p^*\nu\kappa_s}$
κ_t				$3+2\delta_q$		
κ_s				$1+6\delta_q+4\delta_q^2$		
κ_f				$2(1+\delta_q)^2$		
				$\max\left\{1, \frac{\kappa_s}{\kappa_t}\right\} \leq \kappa^* \leq \frac{2\kappa_s}{\kappa_f}$		
	MR1			MR2		
κ^*	$\frac{2\kappa_s}{\kappa_f}$			$\frac{1}{15}[15+(15+4\sqrt{3})\delta_q - (4\sqrt{3}-3)\delta_q^2]$		

$$\kappa^*(\delta_q) = 1 + \frac{15+4\sqrt{3}}{15}\delta_q - \frac{4\sqrt{3}-3}{15}\delta_q^2, \quad (56)$$

based on the following heuristic: the function $\kappa^*(\delta_q)$ is quadratic in δ_q , increasing, and goes through the points (0,1), ($\delta_0, 3/2$), and (1,11/5).

F. Summary

Table II and the following results summarize the previous sections.

(1) The linear LB equation with the bounce-back condition gives an exact Couette flow if the planes are parallel to a symmetry plane of the lattice and cut the nonperpendicular links in their middle. The same result applies for Poiseuille flows if Λ^2 is equal to some particular values: 1/4 if the flow is along a main axis.

(2) The linear LB equation with the boundary conditions in Table II, except the bounce-back one, gives the exact solution for any inclined Couette flow.

(3) The linear LB equation with the multireflections gives the exact solution for any inclined Poiseuille flow.

(4) Linear interpolations (24) and (25) are second-order accurate for general flows.

(5) Multireflections with postcorrection (46) are third-order kinetic accurate for general flows.

IV. MOMENTUM TRANSFER ON THE BOUNDARY

A. Classical definition

Let us define the momentum transport $\vec{M}^{(c)}$ on the boundary in the classical way (see Ref. [14,24]) as

$$\vec{M}^{(c)} = \sum_{q \in \mathcal{C}} (\tilde{f}_q(\vec{r}_b) \vec{c}_q - f_{\bar{q}}(\vec{r}_b) \vec{c}_{\bar{q}}) = \sum_{q \in \mathcal{C}} [\tilde{f}_q(\vec{r}_b) + f_{\bar{q}}(\vec{r}_b)] \vec{c}_q, \quad (57)$$

where the sum goes through all the cut links $q \in \mathcal{C}$ for all the boundary nodes \vec{r}_b . Let us denote

$$M_q(\vec{r}) = \tilde{f}_q(\vec{r}) + f_{\bar{q}}(\vec{r}), \quad (58)$$

the sum of Eqs. (A1) and (A2) gives

$$M_q(\vec{r}) = t_p^* \left(2P + \frac{3j_q^2 - j^2}{\tilde{\rho}} + F_q \right) + (2 - \lambda_\nu) f_q^{(1)} - \lambda_2 f_q^{(2)}. \quad (59)$$

Using Eqs. (27) and (28) and the projected stationary Navier-Stokes equation (49), it comes

$$\begin{aligned} M_q(\vec{r}) &= t_p^* \left(2P + \frac{3j_q^2 - j^2}{\tilde{\rho}} - 6\nu \partial_q j_q + \partial_q P \right. \\ &\quad \left. + \partial_q \frac{3j_q^2 - j^2}{2\tilde{\rho}} - 3\nu \partial_{qq} j_q \right) \\ &= M_q^{(b)}(\vec{r} + \frac{1}{2} \vec{c}_q), \end{aligned} \quad (60)$$

where $M_q^{(b)}(\vec{r})$ is defined as

$$M_q^{(b)}(\vec{r}) = 2t_p^* \left(P + \frac{3j_q^2 - j^2}{2\tilde{\rho}} - 3\nu \partial_q j_q \right), \quad (61)$$

the right hand side term being taken at \vec{r} .

If the pressure, nonlinear terms, and momentum derivatives are constant for all $\vec{r}_b + \vec{c}_q/2$, they can be factored in Eq. (57) to give

$$\begin{aligned} \vec{M}^{(c)} &= \left(P - \frac{j^2}{2\tilde{\rho}} \right) \sum_{q \in \mathcal{C}} 2t_p^* \vec{c}_q + \left(\frac{j_\alpha j_\beta}{2\tilde{\rho}} - \nu \partial_\beta j_\alpha \right) \\ &\quad \times \sum_{q \in \mathcal{C}} 6t_p^* c_{i\alpha} c_{i\beta} \vec{c}_q. \end{aligned} \quad (62)$$

For a plane surface going through the points A_{00} , $A_{10} = A_{00} + (l_x, 0, l_z)$, and $A_{01} = A_{00} + (0, m_y, m_z)$, where l_x , l_z , m_y , and m_z are integers, it can be shown that

$$\sum_{q \in \mathcal{C}_S} 2t_p^* \vec{c}_q = A_S \vec{n},$$

$$\sum_{q \in \mathcal{C}_S} 6t_p^* c_{i\alpha} c_{i\beta} c_{i\gamma} = A_S (n_\alpha \delta_{\beta\gamma} + n_\beta \delta_{\alpha\gamma} + n_\gamma \delta_{\alpha\beta}), \quad (63)$$

where \vec{n} is the normal to the surface directed outwards, A_S is the area of the plane surface S limited by the closed path $(A_{00}, A_{10}, A_{11}, A_{01})$ [with $A_{11} = A_{00} + (l_x, m_y, l_z + m_z)$], and \mathcal{C}_S is the set of links cut by S . It follows (using $\vec{\nabla} \cdot \vec{j} = 0$) that $\vec{M}^{(c)}$ restricted to S is given by the classical formula for incompressible flows [41]

$$\vec{M}_S^{(c)} = A_S \left(P \vec{n} + \frac{j_n \vec{j}}{\tilde{\rho}} - \nu (\partial_n \vec{j} + \vec{\nabla} j_n) \right), \quad (64)$$

where $j_n = \vec{j} \cdot \vec{n}$ and ∂_n is the derivative along the normal to the surface.

When the external force is constant and the flow is stationary, it follows from the momentum conservation that

$$\vec{M}^{(c)} = \vec{F} V^l, \quad (65)$$

where V^l is the number of nodes where the force addition $t_p^* \vec{c}_i \cdot \vec{F}$ is applied in Eq. (2). Consequently, $\vec{M}^{(c)}$ is independent of the solution when an external force \vec{F} is used.

B. Modified definition

Let us now give a modified definition of the momentum transport on the boundary

$$\vec{M}^{(n)} = \sum_{q \in \mathcal{C}} M_q^{(b)}(\vec{r}_b + \delta_q \vec{c}_q) \vec{c}_q, \quad (66)$$

where $M_q^{(b)}(\vec{r}_b + \delta_q \vec{c}_q)$ can be computed as

$$M_q^{(b)}(\vec{r}_b + \delta_q \vec{c}_q) = (\frac{1}{2} + \delta_q) M_q(\vec{r}_b) + (\frac{1}{2} - \delta_q) M_q(\vec{r}_b - \vec{c}_q). \quad (67)$$

Indeed relation (67) comes from the following property of any function $f(x)$:

$$f(x + \delta) \approx \frac{1}{2} [(1 + 2\delta)f(x + \frac{1}{2}) + (1 - 2\delta)f(x - \frac{1}{2})]. \quad (68)$$

With the modified definition the momentum exchange is computed on the surface with a second-order accuracy and not in the middle of the cut links as for the classical definition. The difference between the first and second definitions is

$$\vec{M}^{(n)} - \vec{M}^{(c)} = \sum_q (\delta_q - \frac{1}{2}) \partial_q M_q^{(b)}(\vec{r}_b) \vec{c}_q. \quad (69)$$

Note that the modified definition does not verify Eq. (65), in a way similar to the nonconservation of mass by the interpolation and multireflection schemes (see Appendix B for examples).

V. NUMERICAL RESULTS FOR STATIC BOUNDARIES

A. Stokes flow

1. Numerical setup

In order to test accuracy of the different boundary conditions, we compare first the results with the quasianalytical solutions of the stationary Stokes equation (12). At a *macroscopic* level with respect to the level of the Stokes equation, the flow of a single fluid in a porous medium is well described by Darcy's law which relates the flow rate of the fluid \vec{Q} to the applied forcing across the medium in a linear way:

$$\vec{Q} = \frac{1}{\nu} \overline{\mathbf{K}(-\vec{\nabla}P + \vec{F})}, \quad (70)$$

where \mathbf{K} is the permeability tensor of the porous medium and $\overline{\vec{\nabla}P}$ is the mean value of the pressure gradient across it. The flow rate \vec{Q} is usually computed as a volume mean value of the momentum \vec{J} :

$$\vec{Q} = \frac{1}{V_s} \sum_r \vec{J}(\vec{r}). \quad (71)$$

Here, the summation goes through all the points in the computational domain and V_s is equal to the volume of the sample. It can be shown that when the momentum is redefined as in relation (9), \vec{Q} coincides with the mean centered population mass flux $\vec{\Phi}$:

$$\vec{\Phi} = \frac{1}{V_s} \sum_r \vec{\Phi}^p(\vec{r}), \quad (72)$$

$$\Phi_{\alpha}^p(\vec{r}) = \frac{1}{2} \sum_{q=1}^{b_m} [\tilde{f}_i(\vec{r}) + f_i(\vec{r})] c_{i\alpha}. \quad (73)$$

One should keep in mind, however, that expressions (71) and (72) represent crude integration rules which do not take into account the exact boundary position. The permeability can also be derived from the drag \vec{F}^d on the solid

$$\vec{F}^d = -(\overline{\vec{\nabla}P - \vec{F}}), \quad (74)$$

and approximated by the momentum transport $\vec{M}^{(c)}$ or $\vec{M}^{(n)}$ on the boundary as defined in Eq. (57) or Eq. (66).

When the fluid is forced in a given direction α , and $\overline{\vec{\nabla}P} = 0$ (e.g., periodic porous media), the diagonal terms of the permeability tensor \mathbf{K} can be computed as

$$k_{\alpha\alpha} = \frac{\nu Q_{\alpha}}{F_{\alpha}}, \quad \overline{\vec{\nabla}P} = 0. \quad (75)$$

In the following sections the main flow is in the z direction and the permeability k_{zz} is simply denoted k . For the simulations with an external force (Secs. V A 4, V A 5, and V B) only the permeability k in periodic samples is given. For the simulations without external force (Sec. V A 6) the results are given for both the \vec{Q} as defined in Eq. (71) and the drag force $\vec{M}^{(c)}$ as defined in Eq. (57). The relative error for any scalar LB variable s_{LB} with respect to its reference value s_a is computed as

$$E_h^{(r)}(s_{LB}) = \frac{s_{LB}}{s_a} - 1, \quad (76)$$

where the subscript h corresponds to the grid spacing, i.e., the inverse of the number of grid points. Because of the integration errors inherent to relations (71), (72), and (57), these global measurements are affected not only by the errors coming from the LB method and the boundary discretization, but also by these integration errors. We also compare the solutions obtained for the velocity or pressure fields with their reference solutions. The difference between the LB solution for $s_{LB} = \{u_y, u_z, P\}$ and the quasianalytical solution s_a for the same field is computed in L^2 norm:

$$E^{(2)}(s_{LB}) = \sqrt{\sum (s_{LB} - s_a)^2 / \sum s_a^2}, \quad (77)$$

where the sums are taken either over all the boundary points (“b” subscripts) or over the fluid points on the whole grid.

Let us note once more that the simulations at fixed value Λ^2 guarantee the linearity of the the LB Stokes solution (11) with respect to \vec{F}/ν for the bounce-back reflection and multireflection with postcorrection (51). For these boundary conditions the results are given for one value of the viscosity only. With other boundary conditions, the exact position of boundary at second and/or higher orders still changes with the viscosity, leading to abnormal dependency of the permeability on the viscosity. The corresponding error reduces when $\nu \rightarrow 0$, but the computation time to reach the steady state increases then accordingly.

2. Couette and Poiseuille flows

As was said in Secs. III C and III D, Couette and Poiseuille flows must lead to exact solutions for the linear LB equation. For the bounce back and linear and quadratic interpolations, this is possible only when the flow is along the symmetry axes of the lattice and the walls are located at their effective place [set for Poiseuille flows by the values of λ_p and λ_2 , see Eq. (40), or Λ^2 for the bounce-back rule, see Eq. (42)]. For the multireflections given in Table II this is true for any inclination of the flows with respect to the axes and any value of λ_p and λ_2 .

For these flows the differences between the analytical profiles and the numerical ones are only due to the round-off errors. However, it is worth noting that these exact solutions require a strict cancellation of the different error terms. They are therefore extremely sensitive to the details of the actual algorithm. For instance, the forcing term must be exactly implemented as in Eq. (2) and the momentum redefined as in Eq. (9) with $I_f = -1/2$ (both conditions are not satisfied in the algorithm of Ref. [14]). In addition, the nonlinear terms in the equilibrium distribution give nonzero third- and fourth-order derivatives for Poiseuille flows, breaking the exact solution obtained for the linear distribution.

In our opinion, the merit of these academic flows is, first, to illustrate our approach in a simple way, and second, to provide simple tests of the computer implementation of boundary conditions.

3. Flow around random fibers

In order to illustrate the benefit of using a constant value of Λ^2 in a nontrivial case, we use models of periodic fibrous

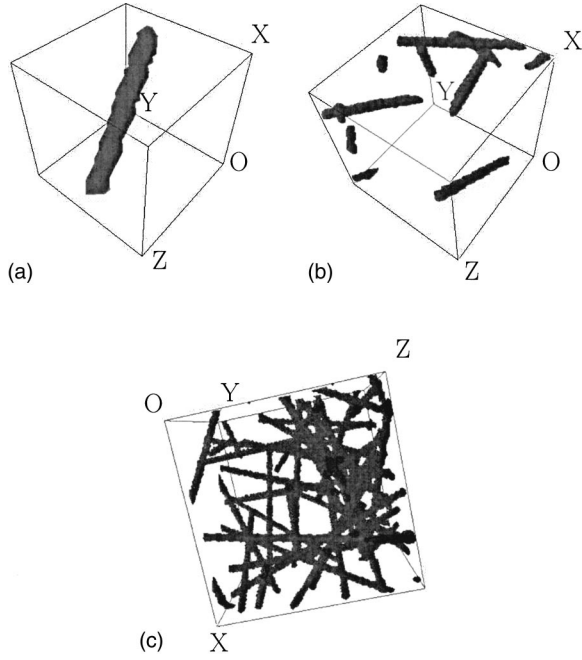


FIG. 2. Fiber materials, from left to right and top to bottom: (a) porosity $\phi \approx 0.965$ in a 20^3 box, (b) porosity $\phi \approx 0.973$ in a 50^3 box, (c) porosity $\phi \approx 0.941$ in a 90^3 box.

material shown in Figs. 2(a)–2(c). The fiber web consists of overlapping cylinders [a single fiber for Fig. 2(a)] of radius equal to 2 lattice units (l.u.). The distribution of the cylinder axes is obtained from a Poisson line process [31]. The measurements are performed with a $D3Q15$ model having one eigenvalue λ_ν for all the even moments and one for all the odd moments (λ_2); the forcing is $F = 2 \times 10^{-6}$ and the boundary condition is the bounce-back rule. We give in Table III first the permeability k_{xx} obtained for the three samples with $\nu = 1/6$ and $\Lambda^2 = 1/4$, then the relative difference in permeability for the case $\Lambda^2 = 1/4$ and for the BGK case ($\lambda_2 = \lambda_\nu$), with $k^{\text{rel}}(\lambda_\nu)$ given by

$$k^{\text{rel}}(\lambda_\nu) = \frac{k_{xx}(\lambda_\nu) - k_{xx}(1)}{k_{xx}(1)}, \quad (78)$$

TABLE III. The third line gives the permeability of the three fiber samples shown in Figs. 2(a) to 2(c) for $\nu = 1/6$. The bottom of the table gives the relative permeability with respect to the previous values for $\Lambda^2 = 1/4$ and the BGK model.

		$20^3, \phi \approx 0.965$		$50^3, \phi \approx 0.973$		$90^3, \phi \approx 0.941$	
ν	λ_ν	k_{xx}		k_{xx}		k_{xx}	
1/6	1	34.0659875		42.249358		26.150806	
		k^{rel}		k^{rel}		k^{rel}	
		$\Lambda^2 = 1/4$	BGK	$\Lambda^2 = 1/4$	BGK	$\Lambda^2 = 1/4$	BGK
		(10^{-12})		(10^{-12})		(10^{-12})	
1/24	8/5	0.1	-0.077	0.1	-0.094	0.1	-0.083
1/6	1	0	0.016	0	0.021	0	0.018
1/2	1/2	0.5	0.311	1.1	0.356		
7/6	1/4	1.3	1.243	-0.3	1.123		
5/2	1/8	-2.8	4.699	0.3	2.946	-0.1	2.236

where $k_{xx}(1)$ is the value of k_{xx} for $\lambda_\nu = 1$ (the choice $\lambda_\nu = 1$ being rather arbitrary).

First we do not want to let the reader believe that we measure the permeability of the samples with an accuracy of few 10^{-13} . We only claim that the viscosity can change by a factor 60 without changing the measured permeabilities by more than $\pm 3 \times 10^{-12}$ when using a constant value of Λ^2 . This is to be contrasted with the BGK case where the permeability is rapidly increasing with the viscosity (by more than a factor 5) as expected from the results for Poiseuille flows. This behavior of the BGK model is in a total contradiction with the physics of Stokes flows.

Finally the results have been obtained for a convergence criteria based on the relative difference between the maximum and the minimum mass flux, the computation ending for a relative difference less than 10^{-6} . Although this criteria is quite stringent, it probably accounts for the 10^{-12} error in the permeability measurements (this error is a few orders of magnitude larger than the numerical round-off ones).

4. Cubic array of spheres

The solution for a viscous flow past a cubic array of spheres [32,33] shows that the drag force F^d on the sphere, exerted by the fluid moving with the average speed \bar{U} , depends on the relative volume solid concentration c as

$$F^d = \frac{6\pi\mu a \bar{U}}{k^*(\chi)}, \quad k = \frac{V_s}{6\pi a} k^*, \quad \chi = (c/c_{\text{max}})^{1/3}, \quad (79)$$

where a is the sphere radius and $c_{\text{max}} = \pi/6$ is the maximal concentration. The function $k^*(\chi)$, inverse of the nondimensional drag, is tabulated in Table 4.9 of Ref. [34]. For a dense array, we use their results (b).

We computed the permeability from relations (71) and (75) and tested the boundary conditions (23)–(25), and (51). The external force is $F = 2 \times 10^{-5}$. The results in Tables IV and V show the relative permeability error with respect to the reference value computed from Eq. (79) and Ref. [34]. The permeabilities in Table IV were obtained for $\tau = 2$, but are independent of the viscosity. Since this is no longer the case

TABLE IV. Comparison of the relative errors on permeability for a cubic array of spheres and the bounce-back and multireflection boundary conditions in a 25^3 box.

χ	$k^*(\chi)$ [34]	Bounce back		Multireflection	
		$E^{(r)}(k)$ (%)	$n/100$	$E^{(r)}(k)$ (%)	$n/100$
0.5	0.35186	-1.02	21	-0.42	22
0.6	0.25165	-2.96	13	-0.46	15
0.7	0.16655	-2.12	9	-0.44	10
0.85	0.07330	1.50	5	-0.35	19
0.90	0.05220	-4.38	4	-0.67	4
0.95	0.03580	-4.28	3	-0.56	5

for the linear interpolations (24) and (25), the corresponding results are given for $\tau=2$ and 0.6 in Table V. The tables include the number of time steps n required to reach a change in k less than 10^{-6} between 10^3 time steps. Note that for the linear interpolations, decreasing the viscosity by a factor 15 increases both the accuracy and the convergence time by almost the same factor.

Note that for the two most dense arrays, situations where some boundary nodes have only one fluid neighbor appear. Despite that, higher accuracy is maintained with the multireflection with postcorrection for all solid fractions.

Although the precision of the linear interpolations in this test is quite satisfactory for small viscosities, it deteriorates when the gap between the spheres approaches 1–2 lattice units. Besides that, the computational time is then 10–20 times higher than for multireflection with postcorrection.

5. Square array of cylinders

For a periodic square array of cylinders, the force exerted on the cylinders per unit length is (see Refs. [32,34,35])

TABLE V. Comparison of the relative errors on permeability for a cubic array of spheres and the linear boundary conditions for $\tau=2$ and 0.6 in a 25^3 box.

χ	$\tau=2$		$\tau=0.6$	
	$E^{(r)}(k)$ (%)	$n/100$	$E^{(r)}(k)$ (%)	$n/100$
0.5	4.28	20	0.88	330
0.6	3.38	14	0.32	230
0.7	3.61	9	0.38	150
0.85	7.73	5	1.68	80
0.90	8.67	4	0.65	70
0.95	10.27	3	1.08	60

$$\frac{F^d}{l} = \frac{4\pi\mu\bar{U}}{k^*(c)}, \quad k = \frac{V_s}{4\pi l} k^*, \quad (80)$$

where l is the cylinder length and c is the relative solid square fraction ($c_{\max} = \pi/4$). The function $k^*(c)$ is tabulated in Table VI (from Table 4.12 of Ref. [34]).

Simulations are similar as above; they are terminated when a change in k is less than 10^{-10} between 10^3 time steps. All computations are done with $\tau=0.875$, $\lambda_2 = -1$ [corresponding to Eq. (43)]. The results with the boundary conditions in forms (23)–(25) and (51) are shown in Tables VI for periodic cells 33^2 and 99^2 .

The results with the coefficients (51) but without the post-correction (46) and with the coefficients (6) from Ref. [14] are shown in Table VII. We would like to stress that they are similar to the results obtained with the linear interpolations, which is not totally surprising since they are all second-order kinetic accurate.

TABLE VI. Comparison of the relative errors on permeability for a square array of cylinders and the bounce-back, linear, and full multireflection boundary conditions on 33^2 and 99^2 grids; r is the cylinder radius.

c	r	$k^*(c)$ [34]	Bounce back	Linear	Multireflection
			k^{rel} (%)	k^{rel} (%)	k^{rel} (%)
33 ² grid					
0.2	8.326		-4.49	-0.04	-0.35
0.3	10.198		-2.59	0.04	-0.35
0.4	11.775		-0.48	1.76	0.05
0.5	13.165		-17.51	-1.36	-0.99
0.6	14.422		-15.56	0.70	-0.45
0.7	15.577		-6.88	22.49	7.50
99 ² grid					
0.2	24.979	2.439×10^{-1}	1.08	0.15	-0.01
0.3	30.593	1.221×10^{-1}	-0.73	0.09	0.03
0.4	35.326	5.767×10^{-2}	-1.43	0.04	-0.02
0.5	39.495	2.360×10^{-2}	-2.83	0.05	-0.03
0.6	43.265	7.128×10^{-3}	-5.27	0.02	-0.11
0.7	46.732	9.295×10^{-4}	0.79	3.79	0.31
0.75	48.372	9.950×10^{-5}	-27.18	6.08	0.79

TABLE VII. Comparison of the relative errors on permeability for a square array of cylinders and the multireflection without the postcorrection and the quadratic interpolation boundary conditions on a 33^2 grid.

c	Multireflection without correction, $E^{(v)}(k)$ (%)	Interpolation (6) from Ref. [14] $E^{(v)}(k)$ (%)
0.2	0.68	0.86
0.3	0.51	0.92
0.4	2.16	2.09
0.5	1.41	2.97
0.6	5.28	5.47
0.7	35.93	28.63

6. Cylinder between moving flat walls

The flow configuration is similar to Ref. [36]. The box is periodic in the x and z directions. Its dimension is $l \times W \times L$. The axis of the cylinder is along the x axis and cuts the $x=0$ plane at (y_0, z_0) referred below as the center of the cylinder; the flat boundaries are found at $y = \pm H$ and are moving in the z direction with velocity $-\vec{u}_w$. This setup simulates a periodic flow in the z direction past an array of cylinders at rest between moving parallel planes. Multipole solution to this problem is discussed in Appendix C. Pressure/velocity/stream function solution is compared with the quasianalytical solution. The lattice Boltzmann results are obtained with the same parameters as for a periodic array of cylinders. The distance δ_q between the flat boundaries and their boundary nodes is put equal to 0.5.

The relative errors of the force and seepage velocity are given in Table VIII. The errors are below 10%; even for the bounce-back condition, most of them are below 1%, especially for the linear interpolation and the multireflection conditions. As for a periodic array of cylinders, it happens first at the concentration 0.6 that a boundary point lacks one point to perform multireflection in a full form. At the concentration 0.7, in addition, some boundary cells are intersected by both boundaries (flat wall and the cylinder). We have found that coefficients (56) are more stable in this situation than coefficients (51). Since the accuracy of coefficients (56) depends on the viscosity, we have chosen here to use a bounce-back condition on a flat wall combined with multireflection on the cylinder for $c=0.7$. In this way, the multireflection/bounce-back solution is still controlled by Λ^2 , but its errors in flow

direction (force, seepage velocity, and u_z) become larger than the error of linear interpolation. Finally, for $c=0.7$, $r=15.57$ here and in the previous test, the bounce-back condition works surprisingly well. Indeed, when the curvature of the cylinder is small, the flow in a gap is close to Poiseuille flow (in the previous test) and to Couette flow (in the current test). Moreover, here the cylinder boundary is shifted at approximately $\delta_q=1/2$ from the last boundary nodes $y = \pm 16$ (since $r=15.57$ and cylinder center $y_0=0$). While applied with $\Lambda^2=1/4$, bounce back and linear interpolation give then quite good results.

The errors between the LB results and the reference solution at the boundary points as a function of their angular position (measured counterclockwise in radian from the z axis) for $c=0.4$ are plotted in Fig. 3 for the pressure and velocity fields. The streamlines are plotted in Fig. 4 for $c=0.4$ (top row) and $c=0.5$ (bottom row). The integration of the velocity fields is done in a similar way for all LB techniques and quasianalytical solution. Table IX summarizes the results based on norm (77) of the error for the pressure and the z and y components of the momentum.

All the simulations reported above have been done in a fully symmetric numerical setup. The LB lift force is then equal to zero and no total mass violation happens with the boundary interpolations. When the center of the sphere/cylinder is shifted from the cell center along the flow direction, these properties do not hold any more. As an example, let us move the cylinder center from the symmetric position on the node $(y_0, z_0)=(18,15)$ to a final position $(y_0, z_0)=(18,15.48)$ close to the middle of a link, with a step increment $(\delta_y, \delta_z)=(0,0.04)$. The box size is 33^2 and the cylinder radius is $R=12$ ($c \approx 0.42$). Figure 5 plots the corresponding mass loss per time step for the linear interpolation and multireflection with postcorrection (there is no mass loss for the bounce-back condition). We see that multireflection with postcorrection has on average a smaller mass loss than the linear interpolation. When mass loss occurs there is no longer any strictly stationary state. However, we have found in our simulations that the momentum field still reaches a steady state (within a stopping criterion of a relative change per time step smaller than 10^{-7}). Hereafter we shall use "stationary regime" for such situations.

Figure 6 shows the relative error in drag force, using its value for the symmetric case $(y_0, z_0)=(18,15)$ as reference. The multireflection with postcorrection is much more accu-

TABLE VIII. Relative error (in %) of the force (left columns) and seepage velocity (right columns) for a square array of cylinders between moving flat walls and the bounce-back, linear, and full multireflection boundary conditions on a 33^2 grid and $\tau=0.875$.

c	Bounce back		Linear		Multireflection	
0.2	2.14	-1.91	7.2×10^{-2}	-0.12	2.6×10^{-2}	-0.11
0.3	1.33	-1.12	5.6×10^{-2}	-0.17	4.8×10^{-2}	-0.21
0.4	-0.43	0.21	-0.71	0.60	-0.19	8.4×10^{-3}
0.5	8.22	-7.91	0.59	-0.93	8.3×10^{-2}	-0.61
0.6	6.14	-6.67	-0.13	-0.15	-0.69	0.16
0.7	0.95	-1.68	1.10	-1.76	5.56	6.39

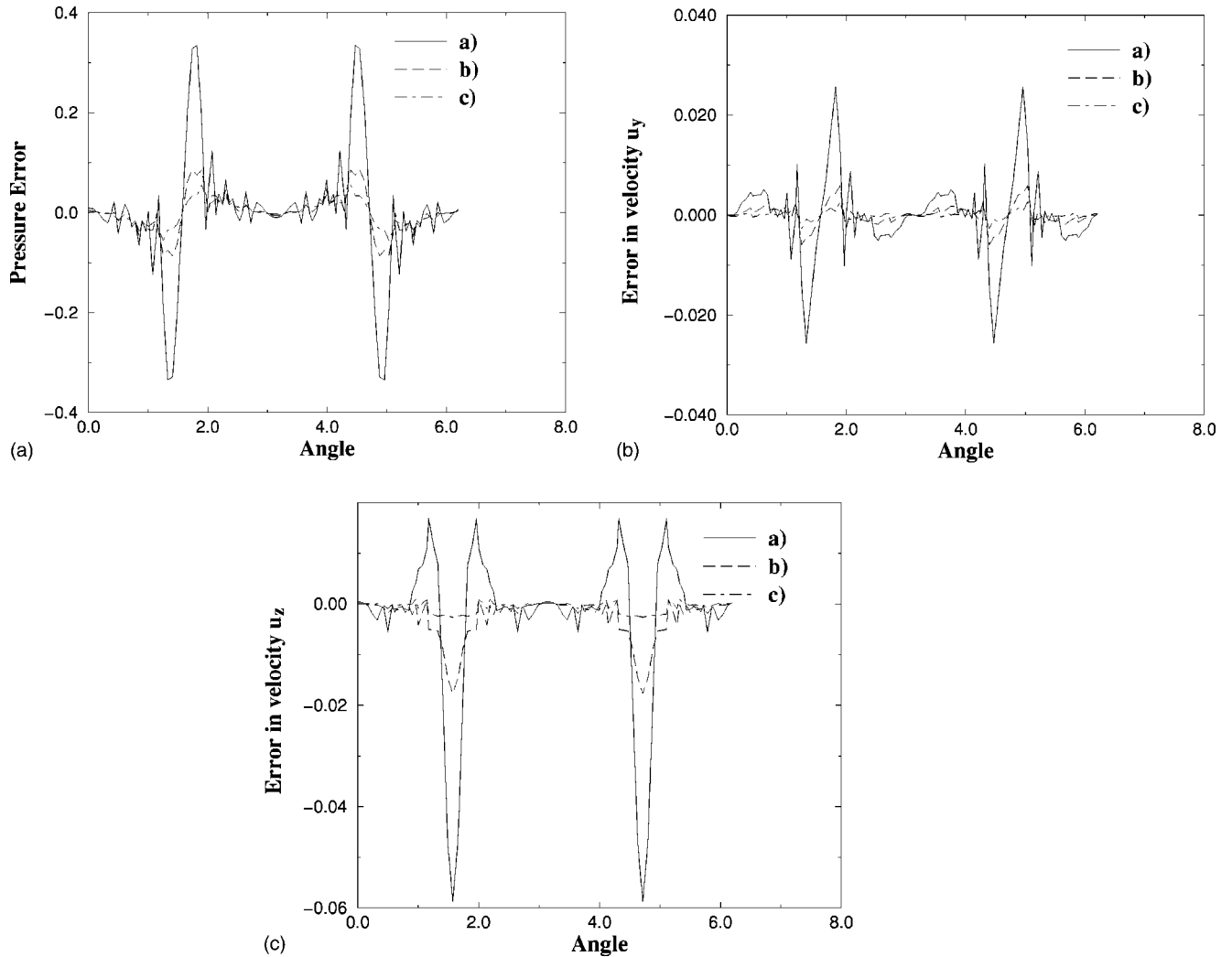


FIG. 3. Error between the LB results and the quasianalytical solution at the boundary points as a function of their angular position (in radian) for $c=0.4$; (a) bounce back, (b) linear interpolation, (c) multireflection. Left to right: pressure rescaled by its max value, y - and z -velocity components rescaled by u_w . The data correspond to streamlines in Fig. 4.

rate than bounce back, and the accuracy for the linear interpolation is usually found between bounce back and multireflection. Note that by definition the error for $(y_0, z_0) = (18, 15)$ is zero and far away from the values displayed in Fig. 6: respectively, 8%, 2%, and 0.15% for bounce back, linear interpolation, and multireflection. Such large values are surprising *a priori*, but we think their explanation is the following. When $(y_0, z_0) = (18, 15)$, in our simulations the points $(6, 15)$ and $(30, 15)$ are considered as solid points of the cylinder; the corresponding links in the z direction are then cut by the boundary [for instance $(30, 15)$ to $(30, 16)$]. When the cylinder center is shifted by a nonzero multiple of (δ_y, δ_z) , these nodes become fluid ones (boundary nodes). The links that were cut in the symmetric case now connect two fluid nodes and are considered as fluid links, although some of them are tangent to the cylinder [for instance $(30, 15)$ to $(30, 16)$]. In our opinion, Fig. 6 illustrates the order of magnitude of the errors caused by a too simple treatment of the links tangent to the boundary surface. It should be noted that multireflection with postcorrection re-

duces considerably the error (an order of magnitude compared to the linear interpolation). A better treatment of these links is left for future work.

7. Summary for Stokes flows

When the exact solution of the studied partial differential equations is not known, a classical estimator of the order p of the numerical scheme is given by the Richardson formula:

$$p = \frac{1}{\ln n} \ln \left(\frac{\phi_{n^2h} - \phi_{nh}}{\phi_{nh} - \phi_h} \right), \quad (81)$$

where ϕ is any measured quantity on grids of mesh sizes h , nh , and n^2h [see Eq. (3.52) page 59 of Ref. [37] for $n = 2$]. When the exact solution is known to be Φ , the same estimate can be computed using only two mesh sizes instead of three, by replacing ϕ_{nh} and ϕ_h by Φ in the numerator and the denominator of the second logarithmic term. In our attempt to extract some convergence order, it turns out that the

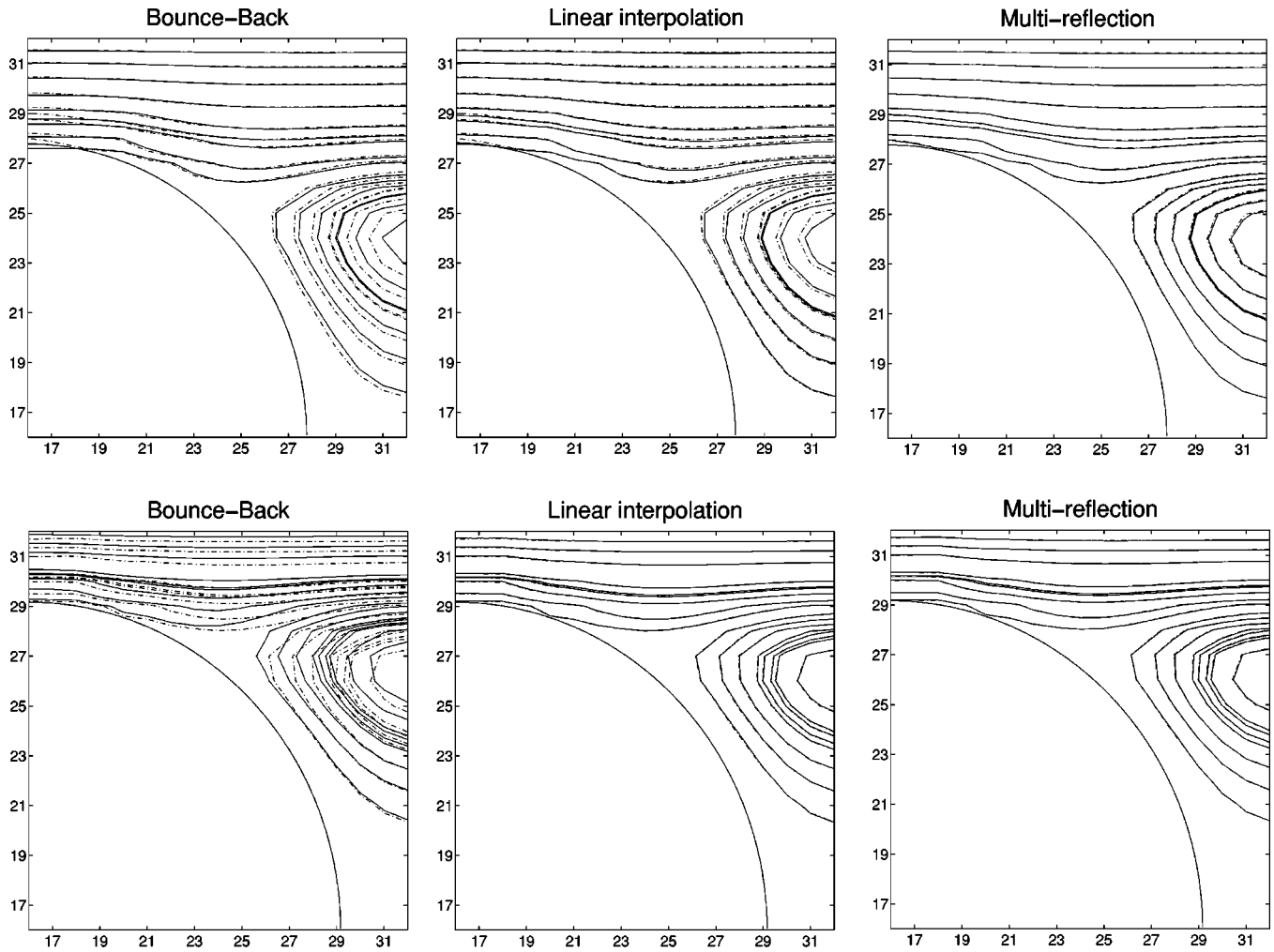


FIG. 4. Streamlines for the flow around a cylinder between flat walls for $c=0.4$ (top row) and $c=0.5$ (bottom row). Left to right: bounce-back method, linear interpolation, and multireflection (solid lines) compared to the quasianalytical solution (dashed lines).

corresponding differences may become negative and we have preferred to use a slightly modified convergence estimator:

$$K_{nh,h}^2 = n^{-2} \frac{E_{nh}^{(r)}(k)}{E_h^{(r)}(k)}. \quad (82)$$

If the accuracy order is p , the value of $K_{nh,h}^2$ should be n^{p-2} , and a second-order accuracy should correspond to $K_{nh,h}^2 = 1$.

This convergence estimator $K_{nh,h}^2(k)$ for the permeability k of the square array of cylinders (Sec. V A 5) is given in Table X for $n=3$. The convergence factors are rather disperse and their values do not reflect the convergence behavior when the coarse grid errors change their sign and/or when they are very close to zero. Note that including the data of Table XI (with $n=1.5$ or 2) does not help.

These results show that the condition stated on page 60 of Ref. [37] is not valid: “The order of convergence estimated using Eq. (3.52) is valid only when the convergence is monotonic.” In our opinion the best support for a nonmonotonic

convergence is given by Fig. 6 of Ref. [14]. It shows that the observed dispersion of the global errors is very large, even for a very extensive numerical test. It seems to us that linear resolutions at least an order of magnitude smaller than ours (three orders more computer time) would be required in order to obtain unquestionable convergence factors. It is even plausible that, due to the effects shown in Fig. 6, the next sentence of Ref. [14]—“Monotonic convergence can be expected only on sufficient fine grids.”—is not even true for our problem and that the convergence will never be monotonic. Then, measuring a convergence order in a reliable way would require a more subtle analysis of the data.

Despite the difficulties to in demonstrating obvious convergence factors, we hope to have shown in a convincing way that the results given in the tables and figures of the previous sections share the following trends.

(1) The errors are significantly smaller for the bulk than for the boundary points, which supports our assumption that the errors are mostly due to the boundary conditions rather than to the approximation of the Stokes equation by the lattice Boltzmann scheme itself.

(2) The errors are significantly larger for the pressure and

TABLE IX. Relative error (77) of the pressure and the momenta in the z and y directions (in %) for the parameters given in Table VIII. Left columns, boundary nodes; right columns, bulk.

c	Bounce back		Linear		Multireflection	
	Pressure					
0.2	13.5	8.6	4.9	3.6	4.2	3.4
0.3	21.2	12.1	6.1	4.0	3.6	3.2
0.4	20.4	15.1	6.5	6.1	3.9	3.9
0.5	19.0	16.5	2.5	2.5	3.5	3.5
0.6	7.5	6.2	6.1	5.7	7.1	6.8
0.7	32.4	28.7	32.0	28.3	30.2	26.7
	Momentum in the z direction					
0.2	19.8	1.86	1.15	0.09	0.49	0.04
0.3	17.2	1.47	1.38	0.15	0.55	0.05
0.4	17.5	1.59	5.82	0.75	1.39	0.20
0.5	24.7	6.59	2.85	0.59	1.02	0.24
0.6	16.1	5.17	3.18	1.20	2.24	1.07
0.7	9.8	5.32	8.86	4.64	13.12	6.67
	Momentum in the y direction					
0.2	20.3	10.8	5.0	1.6	2.4	0.9
0.3	47.7	21.9	5.2	2.3	2.2	0.9
0.4	34.6	27.4	8.9	7.0	3.2	2.2
0.5	39.0	26.1	7.0	3.5	3.9	2.3
0.6	30.6	15.9	9.8	5.2	6.6	4.4
0.7	26.1	14.3	17.5	8.9	13.9	7.1

the y component of the momentum than for the z component of the momentum.

(3) Pressure/velocity fluctuations obtained with the bounce back rule near the cylinder boundary are similar to those described in Ref. [10] for inclined Poiseuille flow. The oscillations are considerably smoothed by linear interpolations and still more by the multireflection.

(4) The linear interpolation improves the overall accuracy by almost an order of magnitude compared to the bounce

TABLE X. Convergence estimator $K_{nh,h}^2$ for the data in Table VI.

c	Bounce back	Linear	Multireflection
0.2	-0.46	-0.03	2.65
0.3	0.40	0.05	-1.48
0.4	0.04	4.82	-0.32
0.5	0.69	-3.21	3.60
0.6	0.33	3.21	0.46
0.7	-0.97	0.66	2.65

back condition, while an additional factor 2 is achieved when the full the multireflection condition is available, i.e., when $c \leq 0.6$ for which the channel width is larger than 3 ($c < 0.6$ for the 33^2 case).

(5) Although the results obtained with linear interpolation can be further improved by decreasing the viscosity, the corresponding computational time is increased quite significantly.

(6) The bounce-back condition provides very satisfactory results for tangential velocity when the flow is dominated by the flow in very narrow straight channels and Λ^2 is fixed close to the value 1/4 (which gives the exact Poiseuille solution).

B. Navier-Stokes flow in a square array of cylinders

The flow configuration here is the same as in Sec. V A 5. Navier-Stokes equilibrium (6) is applied in its incompressible variant [22,23]. Solution for a 66^2 box is computed at solid fractions $c \in \{0.2, 0.6\}$ for Re numbers in the range [0,180]. This interval has been chosen for comparison with the results computed using a stationary finite element (FE) method in Ref. [38] and with a nonstationary FE method in Ref. [39]. Note that these two sets of results differ significantly for $c=0.5$ and $c=0.6$ (see Fig. 8). According to Ghaddar [39], these differences may come from “a lack of resolution due possibly to large iteration or/and discretization

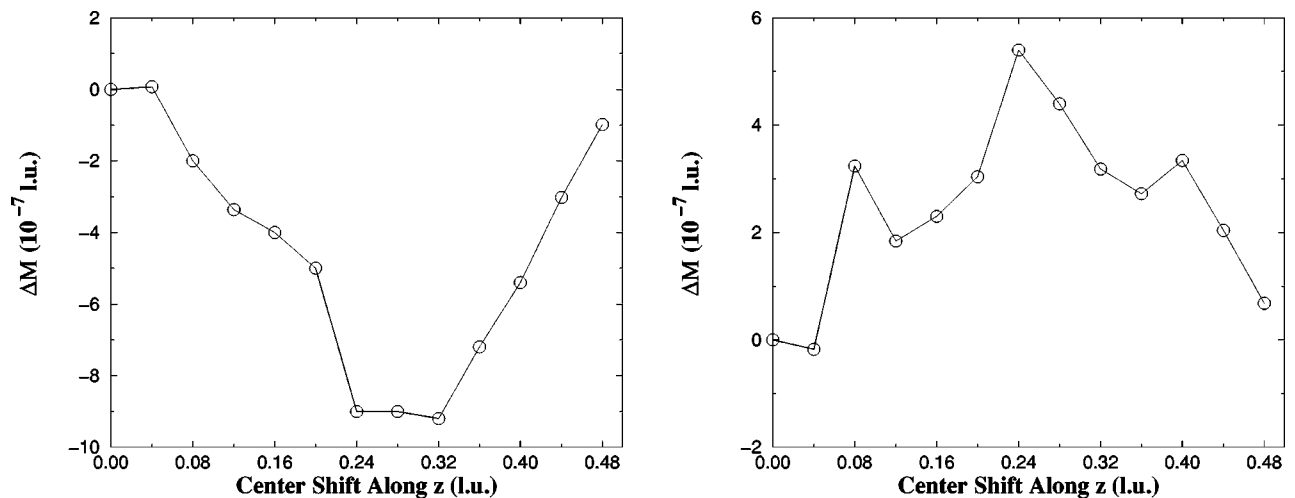


FIG. 5. Mass loss per time step at the stationary regime corresponds to the previous picture. Left: linear interpolation. Right: multireflection with postcorrection.

TABLE XI. Relative permeability error (in %) for the Stokes regime with respect to the reference value (80).

c	Finite element [38]	Bounce back	Linear	Multireflection
0.2	2.54	-1.63	5.5×10^{-2}	-6.5×10^{-2}
0.3	0.53	0.78	0.51	2.8×10^{-2}
0.4	-0.64	-4.86	0.13	-9.2×10^{-2}
0.5	-2.54	-1.1	-0.95	-8.9×10^{-3}
0.6	-8.36	-6.9	0.55	-2.1×10^{-1}

errors” in Ref. [38]. We have also observed a quite strange feature in the data of their Table I: for any Reynolds number the permeabilities for $c=0.5$ are exactly those for $c=0.6$ divided by 0.291 (up to the table accuracy). The LB method with bounce back reflection is also used to simulate this flow in Ref. [40].

Table XI gives for this grid size the relative error $E^{(r)}(k)$ of the Stokes permeability k_S with respect to the reference values computed from Eq. (80) and Ref. [34]. The Stokes solution is obtained with $\Lambda^2=1/4$ and solution (43) at $\tau=1$.

The dimensionless permeabilities are scaled below by the quasianalytical solution [35] in the Stokes regime, except the results of Ghaddar which are scaled by its own Stokes values, being believed “virtually exact” (see Table V in Ref. [39]). They are plotted in Fig. 7 for $c=0.3$ and 0.5. For these fractions, bounce-back solution at the Stokes regime has a relatively small error (see in Table XI). We find then that the Navier-Stokes results are also rather close together for the three boundary techniques. For $c=0.4$, the bounce back results differ significantly from those obtained with the linear interpolations and multireflections. Figures 8 show for each method the effect of scaling the apparent permeability either by the quasianalytical solution (left curve) or by its own value obtained at $\text{Re}=0$ (right curve). When rescaled by its own permeability k_S , the bounce back results approach those obtained with the boundary interpolations. This comparison shows that most of the bounce back error is coming from the 5% error in the Stokes regime.

For the values of $\tau \in [0.53, 0.56]$ used here, the global measurements obtained with the linear interpolations and multireflections in nonlinear regimes are rather close to-

gether. They are also very close to Ghaddar’s solution. Unfortunately, we have not yet found another reference to compare with more accurately for nonlinear flows.

Multireflection provides in a regular manner higher Re numbers than the linear interpolations. Similarly, bounce back solution usually gives an underestimated Re numbers. This is probably related to the fact that the effective radius (square fraction) obtained with bounce back is higher than the expected value. We want also to stress that multireflections with coefficients (56) converge much faster to a stationary state than solution (51). Whereas in the previous tests there was no total mass violation due to the symmetry, in current tests we observe some loss of mass with respect to the initial distribution. For instance, the relative mass loss per time step at a stationary regime for $c=0.5$, $\text{Re} \approx 23$ is 4×10^{-7} by linear interpolation and 2.3×10^{-7} by multireflection. At $\text{Re} \approx 174$, these values are 4.7×10^{-6} and 6×10^{-7} . These data show that the mass violation increases with Re but its absolute values and rates are smaller for the multireflections. Similar results are obtained in other tests.

Table XVI in Appendix D gives the dimensionless apparent permeability $\bar{k}=k/k_S$ values (right columns) versus Re numbers (left columns) for the linear interpolations.

VI. MOVING BOUNDARIES

A. Algorithms

1. Definitions

In order to test the robustness of the linear interpolations (24) and (25) and multireflections (51) and (56) in situations

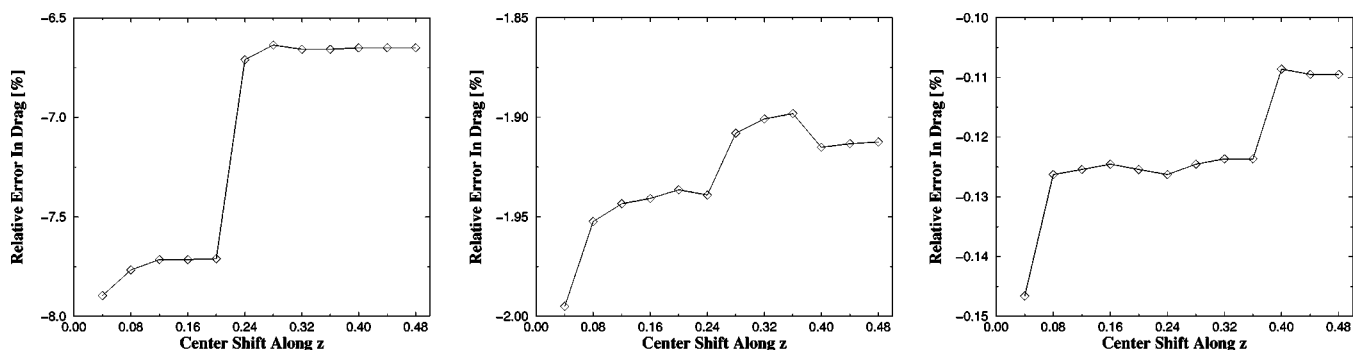


FIG. 6. Relative difference in drag with respect to symmetric cylinder position when its center is shifted along the z axis (l.u.). Left to right: bounce back, linear interpolation, multireflection with postcorrection.

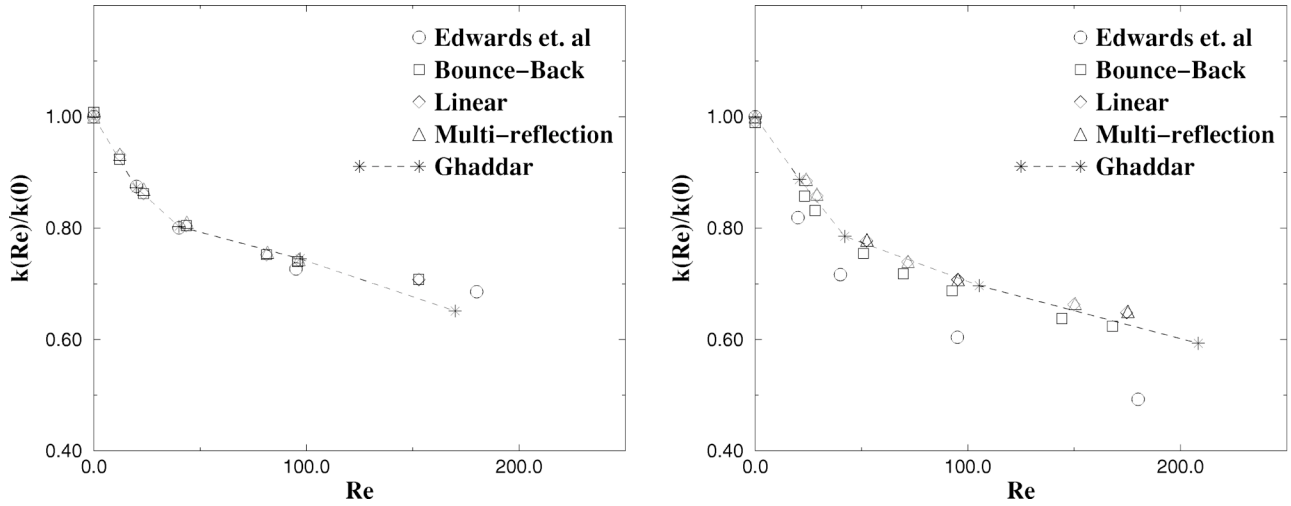


FIG. 7. Dimensionless permeability values vs Re number at $c=0.3$ (left) and $c=0.5$ (right). In both cases, the quasianalytical solution [35] in the Stokes regime is used to rescale the apparent permeability.

where the distance δ_q varies in a natural way, we construct moving boundary algorithms based on these boundary conditions.

The fluid points are defined as in Sec. III A and the other points are called “solid.” It is then natural to divide the corresponding solids into “static” and “moving” ones, depending on the time behavior of their limiting surfaces: a solid is said static if its limiting surface does not change its position on the lattice, and moving otherwise. The points in static and moving solids are respectively called static and moving solid points. Accordingly, at each time step t , the boundary (fluid) points, defined as in Sec. III A, are also divided into static and moving boundary points. The ones which currently have neighbors only in static solids are called *static boundary points* and are handled as described in Sec. III. The boundary points that have at least one neighbor in a moving solid, at link distance δ_q ($0 \leq \delta_q < 1$), are called *moving boundary points* and their treatment is described in the following sections. Fluid, moving solid, and boundary

points of both kinds can exchange their status. The only restriction here is on the velocity of the solid body which must be less than 1 l.u. per time step in any direction so that the fluid/solid points cannot exchange their status without staying at least one time step in the boundary sets.

Note that in our computer implementation the static solid points are actually not stored (allocated), while we have found simpler to store the moving ones in all the following algorithms.

2. Connections to other methods

Starting from any time t our main algorithm goes through the following substeps to get the new state at time $t+1$: collision, propagation, boundary conditions, analysis, advection of the moving solids, and reconstruction of new fluid points. The first four steps are identical to those used in Sec. V. The solid advection corresponds to a sampling of the position of the moving solids at a time $t^{ad} = t + \Delta_t^{ad}$, with 0

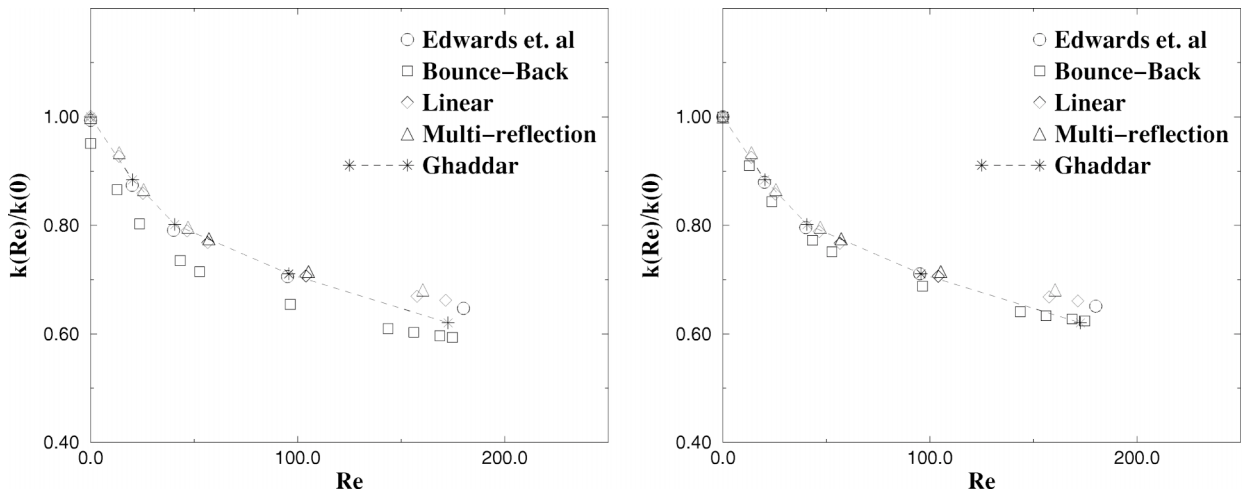


FIG. 8. Dimensionless permeability values vs Re number for $c=0.4$. Left: the permeability is scaled by the quasianalytical solution [35] in the Stokes regime. Right: the permeability for each method is scaled by its own value in the Stokes regime.

$\leq \Delta_t^{ad} \leq 1$. As a result of this advection step some fluid points become solid and some solid points become fluid. The state of these new boundary (fluid) points has to be supplied and in the available literature this is done along two main lines.

Along the first one (see, for instance, Refs. [36,43]), called the LB in fluid technique in the sequel, the LB equations (1) and (2) are applied only in fluid points. The difficulty of this approach is that all the populations in the new boundary points have to be reconstructed. In Ref. [43], the equilibrium distribution with the mean density of the surrounding fluid and the velocity of the solid body was used. In Ref. [36], all the populations were interpolated from bulk with second-order schemes. In our implementation we try to stay as close as possible to the static LB algorithm. We first obtain all possible populations by the advection step (1). Then the links opposite to the new cut ones are reconstructed using relation (22) with some necessary interpolations discussed in the following section. Finally, the remaining populations, called ‘‘tangential’’ below, are reconstructed explicitly (the second part of the following section).

Along the second line (see, for instance Refs. [25,44]), called LB in solid in the sequel, the collision and propagation steps are applied in all the fluid and moving solid points (though the populations are recomputed as an equilibrium in Ref. [44]) and the state of the new fluid points is automatically supplied by the value they had in the solid. In addition the boundary conditions are applied on both (concave and convex) sides of the solid boundary in Refs. [25,44]. In our LB in solid implementation the collision and propagation steps are applied unchanged everywhere. In particular the propagation takes place from fluid points to the solid ones according to the evolution equation (1) which, in our opinion, supplies the continuation of the solution from the fluid to the solid. When a solid point becomes a boundary fluid point, its populations along the links from fluid to solid are already obtained from the advection step and the opposite cut links are reconstructed exactly as in our LB in fluid algorithm above (we have noticed that using the value they had in the solid leads to larger fluctuations of the solution). The other (tangential) links are the only ones actually keeping their value from the solid.

We compute the force according to Eq. (57) or Eq. (65) during the analysis step, before the points change their status from solid to fluid. This has to be contrasted with the computation of the force contribution from new fluid/solid points described in Refs. [43,44]. Note also that in both our moving methods, the boundary conditions are applied only in the boundary fluid nodes.

Finally in the examples given in Sec. VI B, the dynamic of the solid objects does not depend on the computed forces, i.e., their velocity is prescribed. Further tests are required to evaluate our moving algorithms (especially the LB in solid one) when the solid dynamics depends on the fluid solution.

3. Details of the moving schemes

Similarities between the LB in fluid and LB in solid algorithms. The key point of our moving algorithm is the distinction between the ‘‘tangential’’ and ‘‘nontangential’’ links in the new fluid points. A link q belongs to the set of tangential

links $\mathcal{T}(\vec{r}_b)$, if $\vec{r}_b - \vec{c}_q$ is also a new boundary fluid point or when both neighbors $\vec{r}_b + \vec{c}_q$ and $\vec{r}_b + \vec{c}_{-q}$ are solid (i.e., \vec{r}_b is in a corner or a narrow channel). Note that $\mathcal{T}(\vec{r}_b)$ always contains the zero velocity \vec{c}_0 . Otherwise, the link is a nontangential link and belongs to the set $\overline{\mathcal{T}}(\vec{r}_b)$ [with $\mathcal{C}(\vec{r}_b) \subset \overline{\mathcal{T}}(\vec{r}_b)$].

The treatment of the nontangential links is exactly the same for the LB in fluid and LB in solid algorithms. When $\vec{r}_b - \vec{c}_q$ is a fluid point, we set $f_q(\vec{r}_b, t+1)$ according to the propagation step (1):

$$f_q(\vec{r}_b, t+1) = \tilde{f}_q(\vec{r}_b - \vec{c}_q, t). \quad (83)$$

When $\vec{r}_b + \vec{c}_q$ belongs to a solid, we set $f_q^-(\vec{r}_b, t+1)$ according to the boundary rules. However, since the postcollision population $\tilde{f}_q(\vec{r}_b, t)$ is not known at the new fluid point, one cannot use directly the bounce-back, linear interpolation or multireflection boundary conditions. For the multireflection cases, one could bring the interpolation coefficient κ_1 to zero with the help of transformations (48) without loss of kinetic accuracy. However, the resulting coefficients are not always found in the ‘‘stability interval’’ $[-1; 1]$. In order to keep similar algorithms for all the boundary techniques under consideration, we interpolate $\tilde{f}_q(\vec{r}_b, t)$ from the bulk. For multireflections, we have also to interpolate the second-order postcollision term $\lambda_2 \tilde{f}_q^{(2)}$ [see Eq. (46)]. The low-order interpolations

$$\tilde{f}_q(\vec{r}_b, t) \approx 2\tilde{f}_q(\vec{r}_b + \vec{c}_q, t) - f_q(\vec{r}_b + \vec{c}_q, t) + O(\epsilon^2),$$

$$\tilde{f}_q^{(2)}(\vec{r}_b, t) \approx \tilde{f}_q^{(2)}(\vec{r}_b + \vec{c}_q, t) + O(\epsilon^3), \quad (84)$$

are used to keep a minimal number of the communications between the neighboring points. In a similar way, we set $\tilde{\rho}$ in relations (6) and (20) equal to the arithmetical mean value $\bar{\rho}$, computed from the neighbor values $\rho(\vec{r}_b + \vec{c}_q)$, $\bar{q} \in \mathcal{C}(\vec{r}_b) \cup \mathcal{T}(\vec{r}_b)$. In addition, for downwind linear interpolation and multireflection, $\tilde{f}_q^-(\vec{r}_b, t)$ is set to $f_q^-(\vec{r}_b - \vec{c}_q, t+1)$. Then the relations (24) or (25) and multireflections (51) or (56) can be used to compute the populations $f_q^-(\vec{r}_b)$ according to relation (22).

Differences between the LB in fluid and LB in solid algorithms. The only difference between our two algorithms is the treatment of the tangential links. In the LB in solid algorithm, the tangential populations keep the values they have obtained in the solid. In the LB in fluid algorithm they are computed assuming all the tangential links at equilibrium. Our heuristic assumes an incompressible flow for which the first-order (27) and second-order (28) corrections of f_0 are equal to zero. In a similar way, the projection of the momentum derivatives (i.e., the first- and second-order corrections) on the other tangential links can be neglected, otherwise the connected points would not appear from the solid at the same time.

TABLE XII. Comparison for a $1 \times 99 \times 201$ box, $\tau=0.875$, of linear interpolations (*A*), multireflections (*B*), multireflections without correction (*C*), multireflections for the LB in solid algorithm (*D*).

	<i>A</i>	<i>B</i>	<i>C</i>	<i>D</i>
$E^{(2)}(p)$ (%)	2.16	0.81	2.4	5.31
$E^{(2)}(u_z)$ (%)	4.40	2.20	5.4	2.52
$E^{(2)}(u_y)$ (%)	1.81	0.05	0.16	0.05
Force at disk				
Static F_y	-0.024	-0.024	-0.024	-0.024
Static F_z	0.62	0.62	0.62	0.62
$E^{(r)}(\bar{F}_y)$ (%)	5.7×10^{-3}	6×10^{-4}	1.6×10^{-2}	0
$E^{(r)}(\bar{F}_z)$ (%)	0.34	0.26	0.37	0.26
$E^{(r)}(F_y)$ (%)	4.5×10^{-3}	2.6×10^{-3}	3×10^{-3}	2.6×10^{-3}
$E^{(r)}(F_z)$ (%)	2.5	0.56	0.57	0.95
Force at flat				
$E^{(r)}(\bar{F}_y)$ (%)	4.4×10^{-3}	7×10^{-4}	1.1×10^{-3}	0
$E^{(r)}(\bar{F}_z)$ (%)	0.29	0.08	3.6×10^{-2}	0.09
Mass loss per period	2.9×10^{-7}	1.4×10^{-8}	3.2×10^{-7}	2.8×10^{-7}

In order to compute the equilibrium in the new fluid points, one has to estimate \vec{J} and ρ . A first-order approximation of the velocity $\vec{u}^{\text{ap}}(\vec{r}_b, t+1)$ is obtained from the arithmetical mean of the linear interpolations between the known values of the velocity $\vec{u}_w(\vec{r}_b + \delta_q \vec{c}_q, t)$ at the boundary and $\vec{u}(\vec{r}_b - \vec{c}_q, t)$ for all $q \in \vec{T}(\vec{r}_b)$ [the boundary velocity is used if $\vec{T}(\vec{r}_b)$ is empty]. Assuming then the equilibrium solution for the tangential links, the unknown density is derived from the linear equation:

$$\rho \left\{ 1 - \sum_{q \in T} f_q^{eq}(1, \vec{u}^{\text{ap}}) \right\} = \sum_{q \notin T} f_q - \frac{1}{2} \sum_{q \in T} t_p^* \vec{c}_q \cdot \vec{F}. \quad (85)$$

We have found that relation (85) leads to slightly smaller oscillations in the solution than the direct use of the approximate density value at equilibrium. Noting that the values $\vec{u}(\vec{r}_b - \vec{c}_q, t+1)$ in the “old” fluid points are already known during the reconstruction of the tangential links, their values could be used instead of $\vec{u}(\vec{r}_b - \vec{c}_q, t)$. However, we have not detected any further improvement of the accuracy with this change.

B. Numerical results

1. Setup for moving boundary tests

In the first setup we simulate a periodic flow past a cylinder (sphere) at rest, the velocity of flat (cylindrical) outer boundary being $-\vec{u}_w$. Hereafter refer to this setup as the static solution (shortly “*s*”). In static and linear regimes, a cylinder between flat walls is considered in Sec. V A 6. The quasianalytical Stokes solution for a sphere traveling along the cylinder axis is considered in Ref. [42]. Static LB solutions are compared with it in Ref. [20]. In the second setup,

an impulsively started cylinder (sphere) moves with velocity \vec{u}_w and the outer boundary is at rest. When the moving solid reaches the box boundaries, its position is adjusted by periodicity. Hereafter we refer to this setup as the moving solution (or simply “*m*”).

As in Ref. [36], we check for the Galilean invariance of the method by comparing the results of the first and second setups when the solids move with a constant velocity and the position of their center of mass \vec{r}_c is given by

$$\vec{r}_c(t^{ad}) = \vec{r}_c(\Delta_t^{ad}) + \vec{u}_w t, \quad t \geq 0. \quad (86)$$

If the flows are Galilean invariant we expect to obtain the velocity, pressure distributions, and forces as

$$\vec{u}^{(s)} = \vec{u}^{(m)} - \vec{u}_w, \quad P^{(s)} = P^{(m)}, \quad \vec{F}^{(s)} = \vec{F}^{(m)}, \quad (87)$$

where $P^{(s)}$ and $P^{(m)}$ are the pressure distributions minus some characteristic mean pressures. The forces are computed independently, once on the outer boundary and once on the inner solid, using the standard definition (57) or the force definition with boundary fitting (66). Since no external force is applied, the sum of the forces on the internal and external boundaries is expected to be zero for the stationary solutions. In order to check relations (87), we measure the values of the velocity and pressure when the moving solid is found at the same position as in the *s* case. We compare also the *m* forces and their averages during one period with their *s* counterparts. Here the period is defined as the minimal number of time steps required to move the solid to the same position, up to an integer displacement, with respect to the underlying lattice (assuming a rational value for \vec{u}_w).

When the solid body moves, the LB solution is no longer stationary in the lattice frame. Since the unsteady Stokes

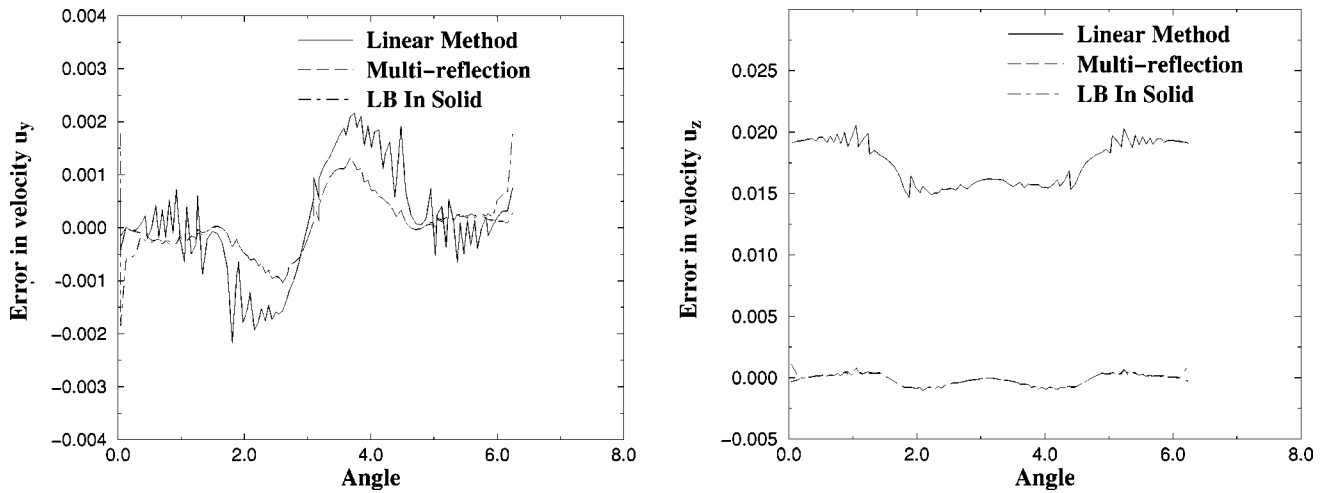


FIG. 9. Relative difference between the moving and static velocities at the boundary points as a function of their angular position (in radian) for a $1 \times 99 \times 201$ box and $\tau=0.875$. “Linear Method” and “Multireflection” correspond to linear interpolations and multireflections for the LB in fluid method; “LB in Solid” corresponds to multireflection for the LB in solid method.

equation does not possess Galilean invariance, we simulate the Navier-Stokes equation in m and s cases (even for small Re numbers). In the following sections our attention will be mostly focused on the LB in fluid algorithm and comparisons with the LB in solid one will be done for the multireflection case only.

2. Impulsively started cylinder in a channel

We consider a $1 \times 99 \times 201$ channel, periodic in the x and z directions. A cylinder, of radius $R=12$ and axis along the x direction, is moving along the z axis with a velocity $u_w = -0.04$. The cylinder starts at $t=0$ from the point $(y, z) = (53.5, 29.65)$ and the time shift $\Delta_t^{ad} = 0.5$.

Case $Re=7$. A stationary static solution is obtained for $\tau=0.875$. The corresponding moving solution is compared with the static one at $t=150\,743$ in point $(y_c, z_c) = (53.5, 29.99)$, when the cylinder finishes its 30th trip through the channel. Table XII shows the relative error estimations (77) between static and moving solutions for pres-

sure and velocity. Figures 9 and 10 show velocity and pressure error distributions at boundary points around the cylinder as a function of their angular position (in radian). Linear interpolations lead to larger difference between s and m solutions. In the case of multireflection, the algorithms with and without internal fluid give very close results except for the points that have just changed their status from solid to liquid. For the LB in solid algorithm and $(y_c, z_c) = (53.5, 29.99)$, such points happen at the rear of the cylinder. The pressure in these points differs strongly from the bulk value [see Fig. 10, LB in solid (1)] and contributes mainly to the pressure error. When no new point appears, the pressure fluctuations are twice smaller [see Fig. 10, LB in solid (2)] and the corresponding $E^{(2)}(p)$ decreases from 5% to 3%. The comparison of the columns B and D in Table XII confirms that the reconstruction of the tangential populations leads to smoother bulk solutions than its “in solid” counterpart.

Table XII shows also the values of the forces in the static regime, the force on the flat wall being exactly the opposite

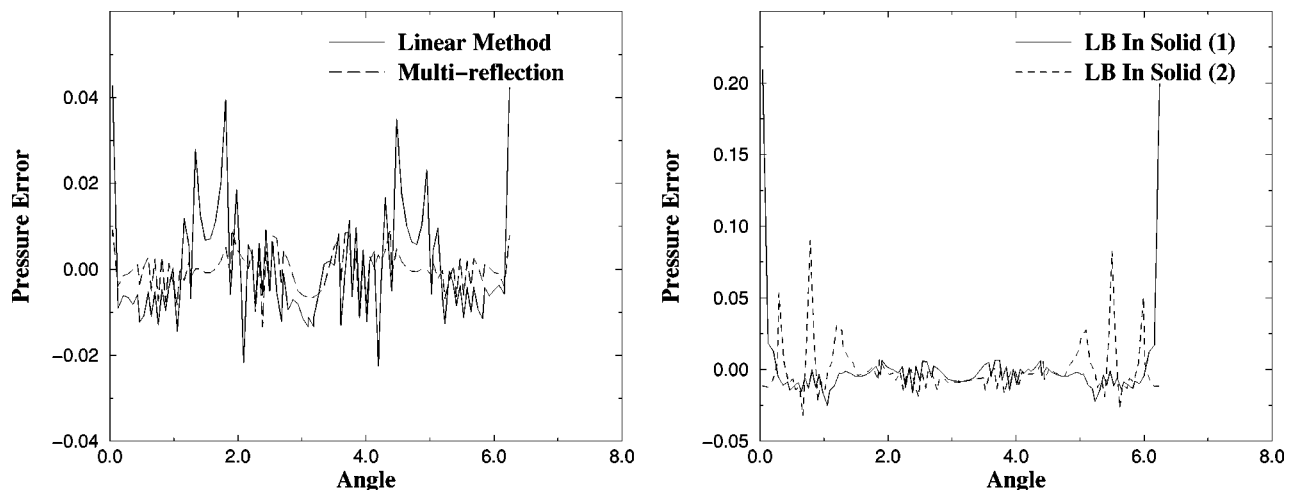


FIG. 10. Relative pressure error corresponding to Fig. 9.

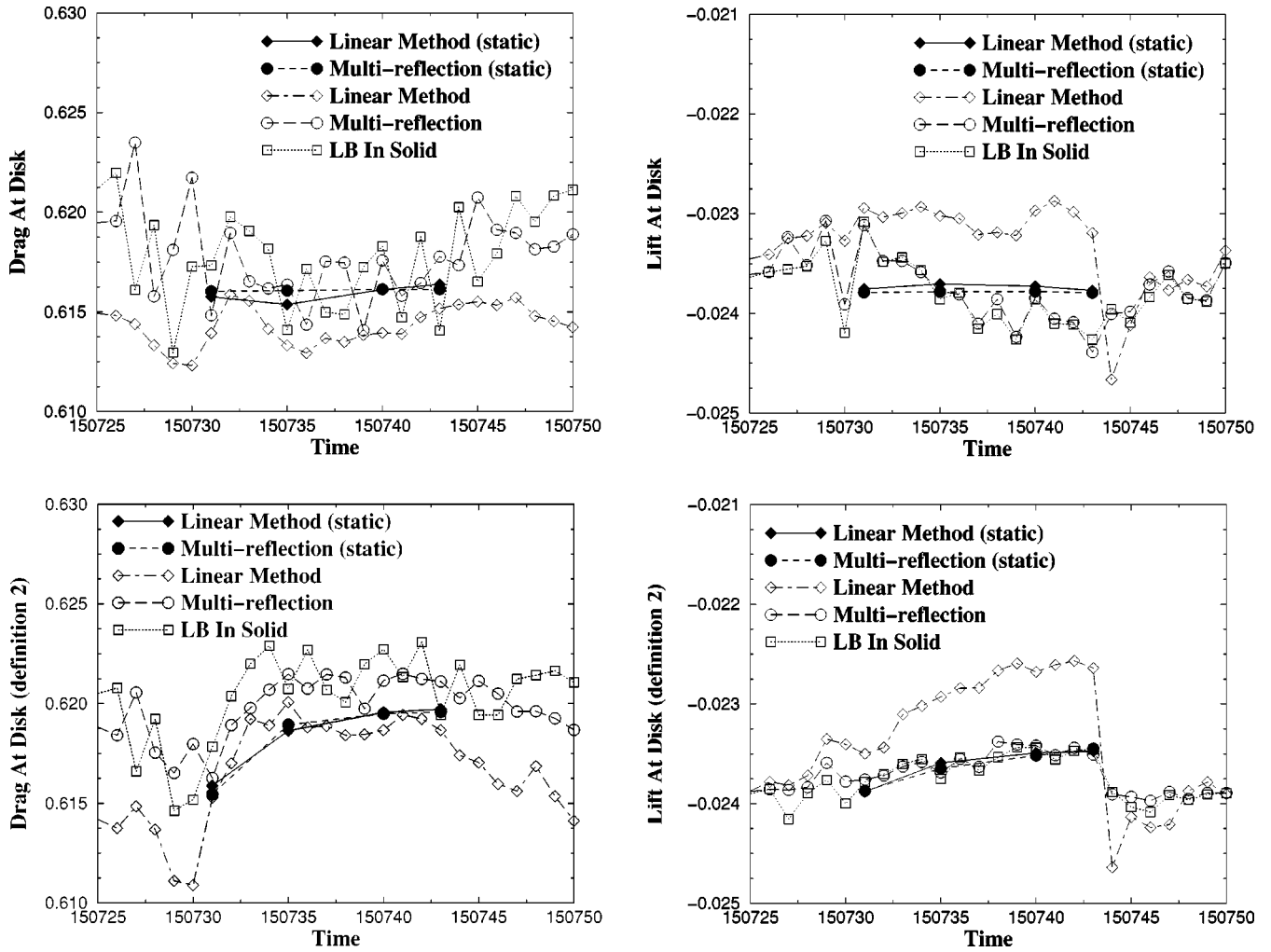


FIG. 11. Drag and lift forces at disk, computed from Eq. (57) (upper row) and Eq. (66) (lower row) are plotted during one period.

of the force on the disk. The relative differences (76) between the static and moving forces [$E^{(r)}(F_y)$ and $E^{(r)}(F_z)$] and the difference between the s force at (y_c, z_c) and the m force averaged over one period (here 25 time steps) [$E^{(r)}(\bar{F}_y)$ and $E^{(r)}(\bar{F}_z)$] are also given. This last comparison is justified if the force changes weakly in the static regime compared with the moving one when the cylinder center shifts within one lattice unit. This is the case here as demonstrated in Fig. 11 where the lift and drag distributions during one period are shown for the moving case (for comparison the static solution is also given for some cylinder positions). The upper and lower rows correspond, respectively, to the force definitions (57) and (66). In the static case, as for the Stokes results of Sec. V A 5, force (57) fluctuations are bigger for the linear interpolations than for the multireflections. In the moving case, the oscillations of both methods are similar for the drag. For the lift, they are stronger for the linear interpolations than with the multireflections. Also, whereas the multireflection solution fluctuates around its corresponding static value, the linear interpolation solution deviates from it.

Case $Re=200$. When $\tau=0.5144$, the solution is no longer stationary. It appears an almost periodic-doubling pat-

tern for the drag (probably due to the fact that the cylinder axis is slightly off the middle of the two flat walls) and an almost periodic one for the lift (it is difficult to be more precise since the final regime has not yet been reached at the end of the simulations). The left column in Figs. 12 and 13 shows drag and lift forces as functions of time computed with definition (57) at cylinder boundary and the right one shows the same quantities but computed with definition (66). Since the flat walls are located at a distance equal to 0.5 of the nearest lattice nodes, both force definitions coincide for the flat wall. The results are plotted for the static case and three moving techniques: linear interpolations and multireflections for the LB in fluid and LB in solid algorithms. The error estimations are also given in Table XIII. Since the solution is nonstationary, the comparison is only done, without averaging, when the cylinder is at the same location for the static and moving cases.

Some remarks are now in order for $Re=200$. First, when the forces are computed in the standard way, the multireflection LB in solid algorithm is found to be the most “oscillatory” one, followed by the LB in fluid algorithm, the linear interpolation algorithm giving the “smoothest” results. When the force distribution with boundary fitting (66) is

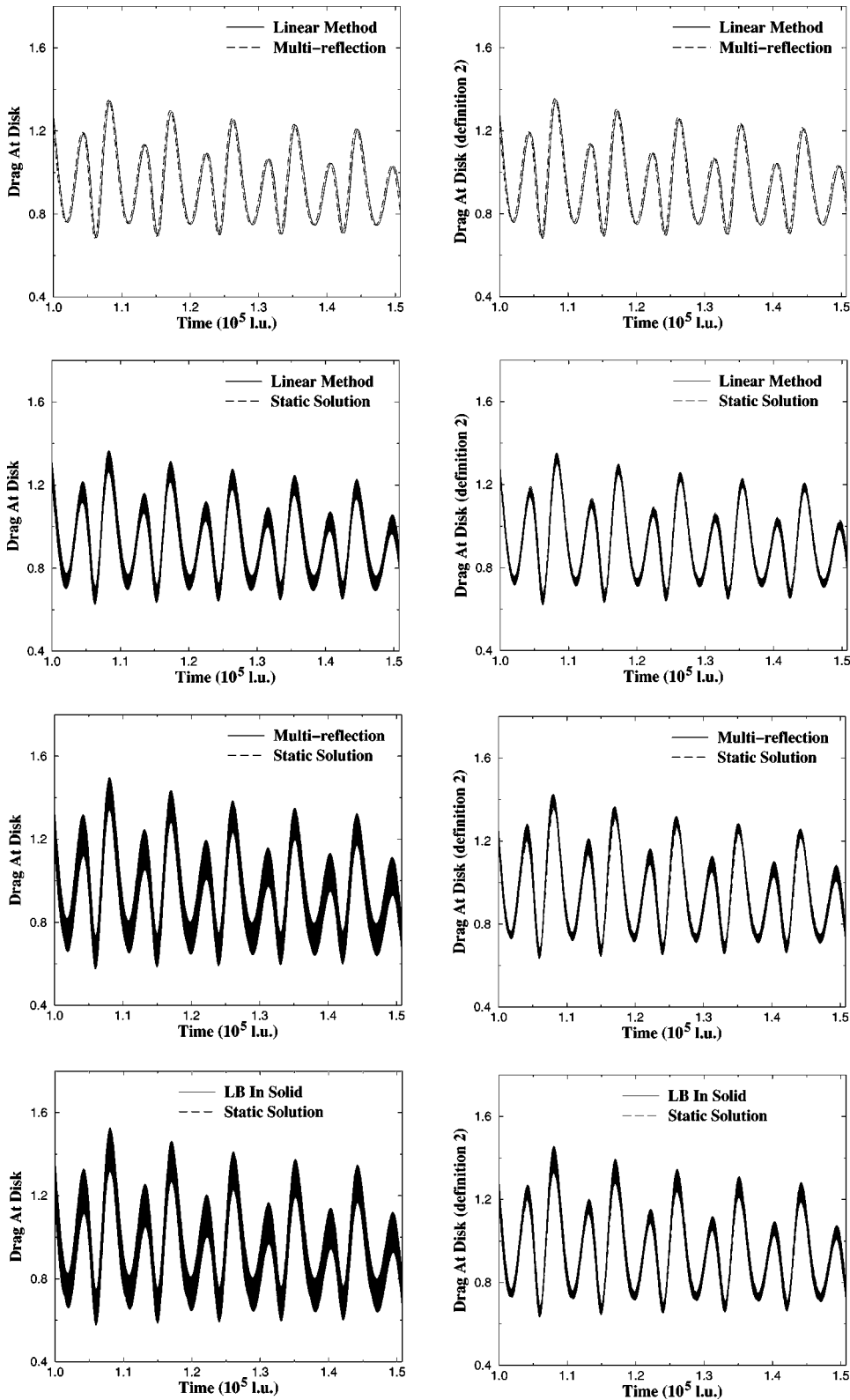


FIG. 12. Drag on the cylinder as a function of time. From top to bottom: “static,” linear reflection, LB in fluid and LB in solid multi-reflection algorithms; the force is computed with definitions (57), left, and (66), right.

used, the smoothness of all solutions, and especially of the LB in fluid algorithm with multireflection, is improved drastically. One technical explanation could be that the force computation (66) involves populations from the next to boundary nodes where the solution fluctuates less. Also, when the surface integration error with Eq. (66) happens to

be smaller than with definition (57), the modified definition improves the computation of forces since the stress values are approximated on the surface. This is also consistent with the fact that the best filtering is achieved for the multireflection algorithms, which have been designed to be the most accurate near the boundaries.

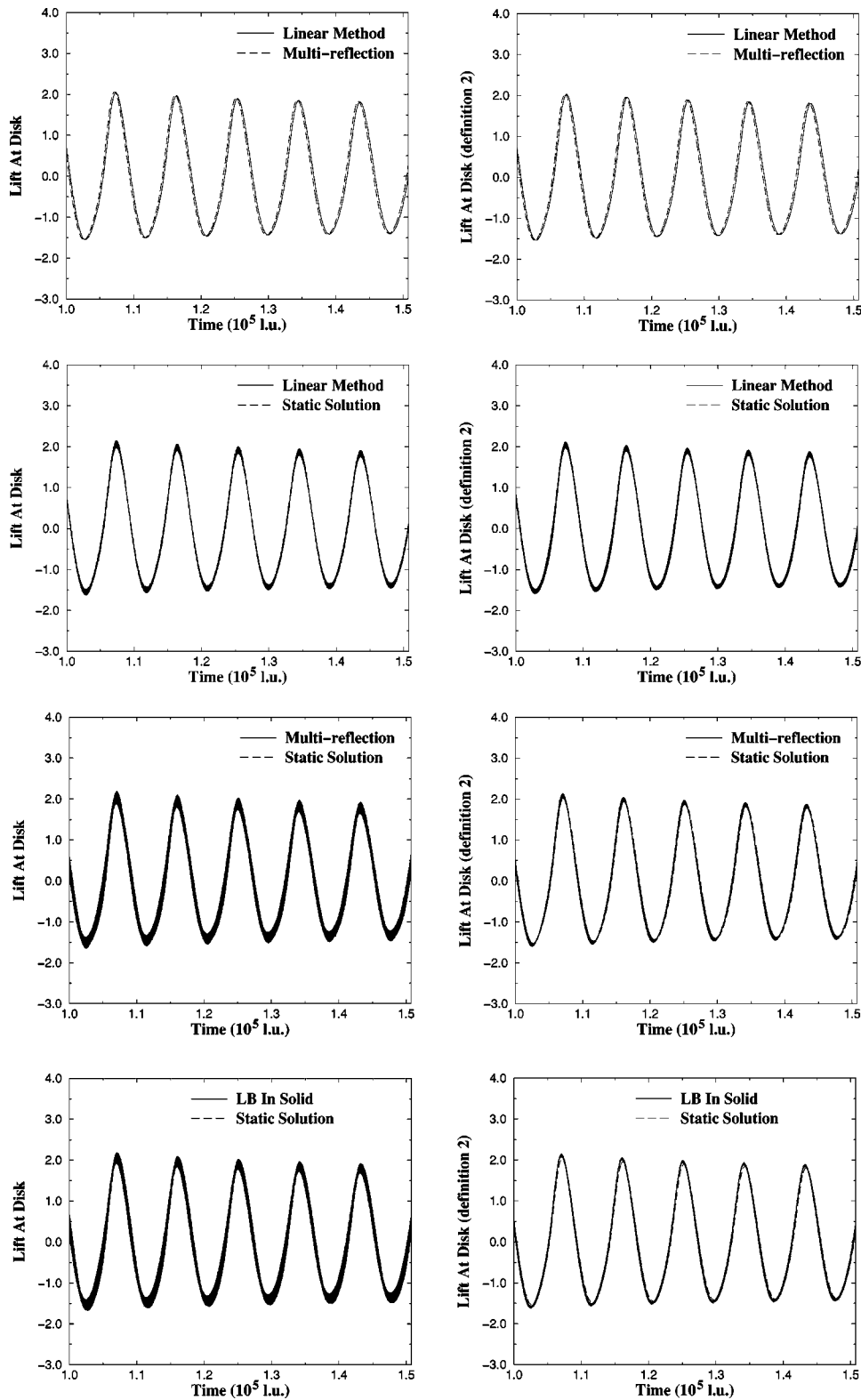


FIG. 13. Lift on the cylinder as a function of time. From top to bottom: “static,” linear reflection, LB in fluid and LB in solid multi-reflection algorithms; the force is computed with definitions (57), left, and (66), right.

3. Moving sphere in a cylinder

We consider a sphere of radius $R_s = 16.9$ in a periodic motion along the x axis of an outer cylinder of radius $R_c = 42.5$ and length $\ell = 189$ along x (in l.u.). The sphere starts from the point $(x_0, y_0, z_0) = (30.65, 4.225, 0)$, with respect to the cylinder axis, and moves with velocity $u_w = -0.04$. The

moving solution is compared with the static one after 31 cycles across the cylinder. Quasistationary solutions are reached in the m and s regimes. The results for forces are shown in Table XIV. The drag and lift values are rescaled by the viscous scaling $\vec{M}^{(i)} / (6\pi\mu\|\vec{u}_w\|Rk^*)$, where k^* is a function of the ratio between the sphere and cylinder

TABLE XIII. Same as Table XII for $\tau=0.5144$.

	A	B	C	D
Force at disk				
Static F_y	1.21×10^{-4}	0.281	0.279	0.281
Static F_z	0.86	0.797	0.797	0.797
$E^{(t)}(F_y)$ (%)	1.62×10^{-2}	1.1×10^{-2}	3.1×10^{-2}	1.0
$E^{(t)}(F_z)$ (%)	3.6	3.78	15	4.77
Force at flat				
Static F_y	3.27×10^{-3}	-0.279	-0.281	-0.278
Static F_z	-0.91	-0.911	-0.911	-0.911
$E^{(t)}(F_y)$ (%)	4.1×10^{-3}	6.7×10^{-2}	0.08	6.7×10^{-2}
$E^{(t)}(F_z)$ (%)	0.21	0.24	0.29	0.24
mass loss per period	2.9×10^{-7}	1.9×10^{-7}	5.2×10^{-7}	1.6×10^{-7}

radii given in Refs. [36,42]. The table shows that in this test the errors on the force are about twice smaller for the multireflection algorithm than for the linear interpolation one.

VII. CONCLUSION

We have shown that boundary conditions based on a link approach such as Ref. [14] can be analyzed in the spirit of Refs. [2–4,10] and their accuracy can be assessed for simple flows such as Couette or Poiseuille-Hagen ones. From this analysis we have been able to derive new boundary conditions for which a third-order kinetic accuracy can be proven theoretically for steady linear or nonlinear LB solutions, leading to the Stokes and Navier-Stokes equations. As a result of this third-order accuracy, linear Couette and Poiseuille flows are exact solutions of the lattice Boltzmann equation

TABLE XIV. Comparison between the static and moving solutions for a sphere in a cylinder at $\tau=0.55$ ($Re=81$) using the linear interpolation and multireflections LB in fluid algorithms.

	Linear	Multireflection
Force at sphere		
Static F_x	0.683	0.688
Static F_y	-3.02×10^{-3}	-3.02×10^{-3}
$E^{(t)}(\bar{F}_x)$ (%)	2.48	1.63
$E^{(t)}(\bar{F}_y)$ (%)	1.7×10^{-3}	0.7×10^{-3}
$E^{(t)}(F_x)$ (%) (at sphere)	1.2	0.56
$E^{(t)}(F_y)$ (%) (at sphere)	4.0×10^{-3}	2.3×10^{-3}
Force at cylinder		
Static F_x	-0.682	-0.689
Static F_y	3.02×10^{-3}	3.02×10^{-3}
$E^{(t)}(\bar{F}_x)$ (%)	2.79	0.54
$E^{(t)}(\bar{F}_y)$ (%)	8×10^{-4}	3×10^{-4}
mass loss per period	3.2×10^{-6}	1.8×10^{-6}

for arbitrary inclination of the flow with respect to the lattice axes.

These exact solutions have been confirmed by numerical simulations of the corresponding flows. In addition several flows in periodic arrays of spheres or cylinders in the Stokes regime and of cylinders for the Navier-Stokes one have been studied. As stated in the Introduction, our goals were set in the context of moderate resolutions and/or moving boundaries and not in the academic context of a convergence factor for an infinite number of grid points. In this context we have confirmed that, as has been found in Ref. [14], the convergence is nonmonotonic and that the usual tools to assess the accuracy order do not work, at least in their naïve implementations. However we think to have shown that the linear interpolation improves the overall accuracy over the bounce-back condition for low viscosities and curved walls. The multireflection method provides a further improvement in the accuracy of the hydrodynamics quantities near the walls for any combination of the collision eigenvalues.

We would like to stress that the bounce-back condition still has several advantages: it is simple, robust, and obeys a strict mass conservation. This is especially true for simulations in complex geometries such as those coming from weakly resolved tomography in which the boundary position is only approximately known. In addition the bounce-back accuracy can be very satisfactory if the following rules are obeyed. First the no-slip condition has to be set in the middle of the cut links. Second the eigenvalues of the collision matrix for the odd and even moments must be chosen such that the corresponding Λ^2 in Eq. (41) is set to a constant value between 1/6 and 1/4: fixed Λ^2 ensures viscosity independent measurements. Also the overall accuracy of the bounce-back condition could be improved for macroscopic quantities through a careful calibration (when available) of the effective boundary locations (see, for instance, Ref. [25]). Note, however, that this calibration does not cure the Knudsen layers near the boundary, but only averages their effects.

The present theoretical analysis, done for steady flows, has to be extended to the unsteady situations. Two theoretical difficulties have also to be studied in more details. First it would be useful to go beyond the heuristic arguments used here to deal with the stability issue. Second it would also be interesting to find a way to keep the accuracy of the multireflection without any mass loss or at least to further investigate its effect. So far we did not see any dramatic effects as long as the quantities rescaled by the density use its actual value at the measurement time. It should also be noted that most methods for moving boundaries suffer some mass loss.

The multireflection scheme requires at least three fluid nodes along a link to be applied. We did not investigate in full detail what happens when this condition is not fulfilled. Among the different possible choices we have looked at, the following recipes have been used. When there are only two fluid nodes, the missing population is taken from its value at the previous time step (see the end of the last paragraph but one of Sec. III A); when there is only one fluid node, we use the bounce back condition. A similar problem, which has also been left for future work, is the case of links tangent to the boundary or cut twice between two adjacent nodes. In

our implementation they are considered as fluid links as long as the end nodes are fluid ones. The effect of different choices remains to be investigated.

Finally, the method has been extended to moving boundaries. As seen by other authors, we confirm that the main difficulty of these simulations comes from an unreliable reconstruction of the pressure in the new fluid points, leading to numerical fluctuations of the physical quantities. Although we have only done a preliminary study, interpolations and multireflections exhibit a surprisingly good overall stability even in changing geometries.

ACKNOWLEDGMENTS

We would like to thank K. Steiner, P. Lallemand, and L.-S. Luo for stimulating discussions. Special thanks are given to P. Klein and M. Beck for numerical help. This work was supported by DFG Project ‘‘Die verallgemeinerte Lattice Boltzmann Methode f ur freie Randwertprobleme und Mehrphasenstr omungen.’’ D.H. also thanks ITWM for its hospitality during this work.

APPENDIX A: TAYLOR EXPANSION FOR BOUNDARY CONDITIONS

In this section we are giving the Taylor expansion for steady solutions of the LB equation. To shorten the formulas the time dependencies are omitted and the right-hand sides are taken at \vec{r}_b . Note also that the second-order derivatives of P and of the nonlinear terms are neglected since they appear at the same order as the third-order derivatives of the momentum,

$$f_q(\vec{r}_b) = t_p^* \left(P - j_q - I_t F_q + \frac{3j_q^2 - j^2}{2\tilde{\rho}} \right) + f_q^{(1)} - f_q^{(2)}, \quad (\text{A1})$$

$$\begin{aligned} \tilde{f}_q(\vec{r}_b) &= t_p^* \left(P + j_q + I_t F_q + \frac{3j_q^2 - j^2}{2\tilde{\rho}} + F_q \right) \\ &+ (1 - \lambda_\nu) f_q^{(1)} + (1 - \lambda_2) f_q^{(2)}, \end{aligned} \quad (\text{A2})$$

$$\begin{aligned} \tilde{f}_q(\vec{r}_b - \vec{c}_q) &= t_p^* \left(P + j_q + I_t F_q + \frac{3j_q^2 - j^2}{2\tilde{\rho}} + F_q \right) \\ &+ (1 - \lambda_\nu) f_q^{(1)} + (1 - \lambda_2) f_q^{(2)} \\ &- 2t_p^* \left[\partial_q P + \partial_q j_q + \partial_q \left(\frac{3j_q^2 - j^2}{2\tilde{\rho}} \right) \right] \\ &+ \frac{1}{2} t_p^* \partial_{qq} j_q - (1 - \lambda_\nu) \partial_q f_q^{(1)}, \end{aligned} \quad (\text{A3})$$

$$\begin{aligned} \tilde{f}_q(\vec{r}_b - 2\vec{c}_q) &= t_p^* \left(P + j_q + I_t F_q + \frac{3j_q^2 - j^2}{2\tilde{\rho}} + F_q \right) \\ &+ (1 - \lambda_\nu) f_q^{(1)} + (1 - \lambda_2) f_q^{(2)} \\ &- 2t_p^* \left[\partial_q P + \partial_q j_q + \partial_q \left(\frac{3j_q^2 - j^2}{2\tilde{\rho}} \right) \right] \\ &+ 2t_p^* \partial_{qq} j_q - 2(1 - \lambda_\nu) \partial_q f_q^{(1)}, \end{aligned} \quad (\text{A4})$$

$$\begin{aligned} \tilde{f}_q(\vec{r}_b) &= t_p^* \left(P - j_q - I_t F_q + \frac{3j_q^2 - j^2}{2\tilde{\rho}} - F_q \right) \\ &+ (1 - \lambda_\nu) f_q^{(1)} - (1 - \lambda_2) f_q^{(2)}, \end{aligned} \quad (\text{A5})$$

$$\begin{aligned} \tilde{f}_q(\vec{r}_b - \vec{c}_q) &= t_p^* \left(P - j_q - I_t F_q + \frac{3j_q^2 - j^2}{2\tilde{\rho}} - F_q \right) \\ &+ (1 - \lambda_\nu) f_q^{(1)} - (1 - \lambda_2) f_q^{(2)} \\ &- t_p^* \left[\partial_q P - \partial_q j_q + \partial_q \left(\frac{3j_q^2 - j^2}{2\tilde{\rho}} \right) \right] \\ &- \frac{1}{2} t_p^* \partial_{qq} j_q - (1 - \lambda_\nu) \partial_q f_q^{(1)}. \end{aligned} \quad (\text{A6})$$

APPENDIX B: EXAMPLES OF MOMENTUM TRANSPORT

1. Noninclined channel

When the force addition in each cell is independent on the position of the boundary (i.e., effective volume of the cell), the momentum transport definition (57) is independent on the actual boundary position [see relation (65)]. Consequently, even if the population f_q is constructed to better fit the boundary, the force $\vec{M}^{(c)}$ will stay the same as for the bounce-back reflection.

Let us illustrate this by the simple example of Poiseuille flow in a channel of width H . If the momentum transport is calculated with definition (57), k is equal to $\nu Q / (FH^l)$, where H^l is the number of liquid points across the channel. Even if the exact value $FH^3 / (12\nu)$ of the flow rate Q is used, the measured permeability is equal to its exact value $H^2 / 12$ only if $H = H^l$, whereas the result is always exact with definition (66).

2. Example: Inclined channel

We consider either a Couette flow,

$$\frac{\partial^2 j_{x'}}{\partial z'^2} = 0, \quad j_{x'}(h') = 1, \quad j_{x'}(-h') = 0, \quad \rho \equiv \rho_0, \quad \vec{\nabla} P \equiv 0, \quad (\text{B1})$$

or a Poiseuille flow

$$-F_{x'} = \nu \frac{\partial^2 j_{x'}}{\partial z'^2}, \quad j_{x'}(\pm h') = 0, \quad \rho \equiv \rho_0, \quad \vec{\nabla} P \equiv 0, \quad (\text{B2})$$

in an inclined channel of width $2h'$, where the coordinates are written in a system rotated to align the x' axis with the flow as

$$\begin{aligned} x' &= x \cos \theta + z \sin \theta, & z' &= -x \sin \theta + z \cos \theta, \\ x &= x' \cos \theta - z' \sin \theta, & z &= x' \sin \theta + z' \cos \theta. \end{aligned} \quad (\text{B3})$$

The exact linear solution is given, for the Couette flow, by

$$N_i(\vec{r}) = t_p^* \left\{ c_s^2 \rho_0 + j_{x'} c_{ix'} + \frac{1}{\lambda_\nu} \frac{\partial j_{x'}}{\partial z'} c_{ix'} c_{iz'} \right\}, \quad i=0, \dots, b_m, \quad (\text{B4})$$

and, for the Poiseuille flow, by

$$N_i(\vec{r}) = t_p^* \left\{ c_s^2 \rho_0 + (j_{x'} + I_{\vec{r}} F_{x'}) c_{ix'} + \frac{1}{\lambda_\nu} \frac{\partial j_{x'}}{\partial z'} c_{ix'} c_{iz'} - \frac{\nu}{\lambda_2} \frac{\partial^2 j_{x'}}{\partial z'^2} c_{ix'} (1 - 3c_{iz'}^2) \right\}, \quad i=0, \dots, b_m. \quad (\text{B5})$$

The substitution of Eqs. (B4) and (B5) into Eqs. (66) and (67), with the help of relation (68), yields at $z' = \pm h'$ the exact result

$$\begin{aligned} \vec{M}^{(n)}(\pm h') &= \sum_{q \in \mathcal{C}(\pm h')} t_p^* \left\{ 2c_s^2 \rho_0 \right. \\ &\quad \left. - 6\nu \frac{\partial j_{x'}}{\partial z'} \Big|_{\pm h'} c_{qx'} c_{qz'} \right\} \vec{c}_q, \end{aligned} \quad (\text{B6})$$

with

$$\nu \frac{\partial j_{x'}}{\partial z'} = \frac{\nu}{2h'} \quad \text{for Couette flow} \quad (\text{B7})$$

TABLE XV. Scaled drag and seepage velocity for a square array of cylinders between moving flat walls as functions of the volume fractions c .

c	$F^d / \mu u_w$	$Q_z / \rho u_w$
0.1	5.34388	0.384425
0.2	6.86103	0.297680
0.3	8.75675	0.232982
0.4	11.4558	0.177666
0.5	15.7519	0.127767
0.6	23.8738	0.0812631
0.7	45.9788	0.0368363

$$\nu \frac{\partial j_{x'}}{\partial z'} \Big|_{\pm h'} = \mp F_{x'} h' \quad \text{for Poiseuille flow.} \quad (\text{B8})$$

For the Couette flow, relation (B6) reads

$$\vec{M}^{(n)}(\pm h') = A_S \left(c_s^2 \rho_0 \vec{n}_\pm \pm \frac{\nu}{2h'} \vec{i}_s \right), \quad (\text{B9})$$

where \vec{n}_\pm are the normal vectors at $z' = \pm h'$ as defined in Sec. IV and \vec{i}_s is the unit vector along the flow. For the Poiseuille flow, relation (B6) reads

$$\vec{M}^{(n)}(\pm h') = A_S (c_s^2 \rho_0 \vec{n}_\pm + F_{x'} h' \vec{i}_s), \quad (\text{B10})$$

then the total momentum transport, $\vec{M}^{(n)} = \vec{M}^{(n)}(-h') + \vec{M}^{(n)}(h') = V^{\text{ef}} F_{x'}$, is equal to the force applied in the *effective volume* $V^{\text{ef}} = 2h' A_S$, whereas it is in the volume V^l , independent of the boundary conditions, when using definition (57).

3. Example: Circular pipe

The solution of the Poisson equation in a circular pipe of radius R is

$$j_y = -\frac{F_y}{4\nu} (r^2 - R^2), \quad r^2 = x^2 + z^2, \quad 0 \leq r \leq R. \quad (\text{B11})$$

For this flow the second-order expansion gives also an exact solution similar to Eq. (B5) and relation (66) is also exact.

TABLE XVI. Re numbers and the corresponding dimensionless apparent permeability $\bar{k} = k/k_S$ values for a 66^2 box; k_S corresponds to Eq. (80).

$c=0.2$	$c=0.3$	$c=0.4$	$c=0.5$	$c=0.6$
22.66	0.86	12.06	0.93	13.64
29.44	0.84	23.26	0.86	25.28
42.56	0.81	43.40	0.80	46.46
67.85	0.77	81.18	0.75	56.52
102.0	0.74	96.12	0.74	104.0
128.4	0.73	124.6	0.72	157.5
151.9	0.72	152.8	0.71	171.4

Since the value of $\nu \partial_r j_y$ at $r=R$ is $-RF_y/2$, definition (66) yields

$$\vec{M}^{(n)} \approx \frac{RF_y}{2} 2\pi R \ell \vec{i}_y, \quad (\text{B12})$$

where ℓ is the length of the cylinder along the y axis. Then the accuracy with the modified definition depends on the evaluation of the surface integral $2\pi R \ell$ in Eq. (B12). Whereas for definition (57), relation (65) reads

$$\vec{M}^{(c)} = F_y V^l \vec{i}_y, \quad (\text{B13})$$

and the precision of the total force computation depends on the accuracy of the discretization of a circle on lattice cells: $V^l/\ell \approx \pi R^2$.

APPENDIX C: MULTIPOLE SOLUTION FOR A FLOW PAST SQUARE ARRAY OF CYLINDERS BETWEEN FLAT WALLS

A quasianalytical solution is obtained from a modification of the multipole procedure [35] to capture Dirichlet conditions at the flat walls. The method is based on the computation of the stream function ψ as a truncated series of terms which are the solution of

$$\Delta^2 \psi = 0, \quad (\text{C1})$$

and satisfy the no-slip condition on the cylinder and the symmetries with respect to its center. The coefficients are then obtained from a least-square fit of boundary conditions at $y=H$ and $z=H$. In Ref. [35] the boundary conditions are $\psi=1$ and $\omega=0$ on the plane $y=H$ and $\partial_z \psi = \partial_z \omega = 0$ on the plane $z=H$ in order to match the periodic conditions and a scaled seepage velocity. In our calculation the boundary conditions are $\partial_y \psi = -\vec{u}_w$ and $\partial_z \psi = 0$ on $y=H$ and $P=0$ and $\partial_z \psi = 0$ on $z=H$.

The only difficulty we have found was a severe loss of accuracy (around one digit per term) when summing the series. We have solved the problem by doing the calculation with the MATHEMATICA software with an intermediate accuracy set to twice the number of terms in the sum. The solution for the drag F^d is normalized as in Eq. (80) and tabulated in Table XV which contains also the seepage velocity value scaled by the wall velocity \vec{u}_w .

APPENDIX D: RELATIVE PERMEABILITY OF A SQUARE ARRAY OF CYLINDERS

As reference values, we give in Table XVI the relative permeability obtained by the LB method with the linear interpolation as described in Sec. V B.

-
- [1] C. Cercignani, *The Boltzmann Equation and Its Applications* (Springer, Berlin, 1988), pp. 252–260.
- [2] R. Cornubert, D. d’Humières, and D. Levermore, *Physica D* **47**, 241 (1991).
- [3] I. Ginzbourg and P.M. Adler, *J. Phys. II* **4**, 191 (1994).
- [4] I. Ginzbourg, Ph.D. thesis, Université Pierre et Marie Curie, Paris, 1994 (unpublished).
- [5] D.P. Ziegler, *J. Stat. Phys.* **71**, 1171 (1993).
- [6] P.A. Skordos, *Phys. Rev. E* **48**, 4823 (1993).
- [7] D.R. Noble, S. Chen, J.G. Georgiadis, and R.O. Buckius, *Phys. Fluids* **7**, 203 (1995).
- [8] D.R. Noble, J.G. Georgiadis, and R.O. Buckius, *J. Stat. Phys.* **81**, 17 (1995).
- [9] T. Inamuro, M. Yoshino, and F. Ogino, *Phys. Fluids* **7**, 2928 (1995).
- [10] I. Ginzbourg and D. d’Humières, *J. Stat. Phys.* **84**, 927 (1996).
- [11] O. Filippova and D. Hänel, *Int. J. Mod. Phys. C* **9**, 1271 (1998).
- [12] H. Chen, C. Teixeira, and K. Molvig, *Int. J. Mod. Phys. C* **9**, 1281 (1998).
- [13] R. Mei, L.-S. Luo, and W. Shyy, *J. Comput. Phys.* **155**, 307 (1999).
- [14] M. Bouzidi, M. Firdaouss, and P. Lallemand, *Phys. Fluids* **13**, 3452 (2001).
- [15] R. Verberg and A.J.C. Ladd, *Phys. Rev. E* **65**, 016701 (2001).
- [16] M. Rohde, J.J. Derksen, and H.E.A. Van den Akker, *Phys. Rev. E* **65**, 056701 (2002).
- [17] D. Yu, R. Mei, L.-S. Luo, and W. Shyy, *Prog. Aerosp. Sci.* **39**, 329 (2003).
- [18] D. d’Humières, *Prog. Astronaut. Aeronaut.* **59**, 450 (1992).
- [19] P. Lallemand and L.-S. Luo, *Phys. Rev. E* **61**, 6546 (2000).
- [20] D. d’Humières, M. Bouzidi, and P. Lallemand, *Phys. Rev. E* **63**, 066702 (2001).
- [21] D. d’Humières, I. Ginzburg, M. Krafczyk, P. Lallemand, and L.-S. Luo, *Philos. Trans. R. Soc. London, Ser. A* **360**, 437 (2002).
- [22] U. Frisch, D. d’Humières, B. Hasslacher, P. Lallemand, Y. Pomeau, and J.P. Rivet, *Complex Syst.* **1**, 649 (1987).
- [23] X. He and L.-S. Luo, *J. Stat. Phys.* **88**, 927 (1997).
- [24] A.J.C. Ladd, *J. Fluid Mech.* **271**, 285 (1994).
- [25] A.J.C. Ladd, *J. Fluid Mech.* **271**, 311 (1994).
- [26] J.M. Buick and C.A. Greated, *Phys. Rev. E* **61**, 5307 (2000).
- [27] Y. Qian, D. d’Humières, and P. Lallemand, *Europhys. Lett.* **17**, 479 (1992).
- [28] H. Chen, S. Chen, and W.H. Matthaeus, *Phys. Rev. A* **45**, R5339 (1992).
- [29] L. Giraud, Ph.D. thesis, Université Pierre et Marie Curie, Paris, 1997 (unpublished).
- [30] R. Cornubert, Ph.D. thesis, Université Pierre et Marie Curie, Paris, 1991 (unpublished).
- [31] D. Reinel-Bitzer, ITWM Annual Report, 1998 (unpublished).
- [32] H. Hasimoto, *J. Fluid Mech.* **5**, 317 (1959).
- [33] A.S. Sangani and A. Acrivos, *Int. J. Multiphase Flow* **8**, 343 (1982).
- [34] P. Adler, *Porous Media: Geometry and Transports* (Butterworth-Heinemann, Stoneham, MA, 1992).
- [35] A.S. Sangani and A. Acrivos, *Int. J. Multiphase Flow* **8**, 193 (1982).
- [36] P. Lallemand and L.-S. Luo, *J. Comput. Phys.* **184**, 406 (2003).
- [37] J.H. Ferziger and M. Peric, *Computational Methods for Fluid*

- Dynamics* (Springer-Verlag, Berlin, 1996).
- [38] D.A. Edwards, M. Shapiro, P. Bar-Yoseph, and M. Shapira, *Phys. Fluids A* **2**, 45 (1990).
- [39] C. Ghaddar, *Phys. Fluids* **7**, 2563 (1995).
- [40] A.J.C. Ladd, *J. Fluid Mech.* **349**, 31 (1997).
- [41] J. Happel and H. Brenner, *Low Reynolds Number Hydrodynamics* (Prentice-Hall, Englewood Cliffs, NJ, 1965).
- [42] M. Tözeren, *J. Fluid Mech.* **129**, 77 (1983).
- [43] C.K. Aidun, Y. Lu, and E.-J. Ding, *J. Fluid Mech.* **373**, 287 (1998).
- [44] M.W. Heemels, M.H.J. Hagen, and C.P. Lowe, *J. Comput. Phys.* **164**, 48 (2000).
- [45] P.L. Bhatnagar, E.P. Gross, and M. Krook, *Phys. Rev.* **94**, 511 (1954).